DANISH METEOROLOGICAL INSTITUTE

SCIENTIFIC REPORT

03-13

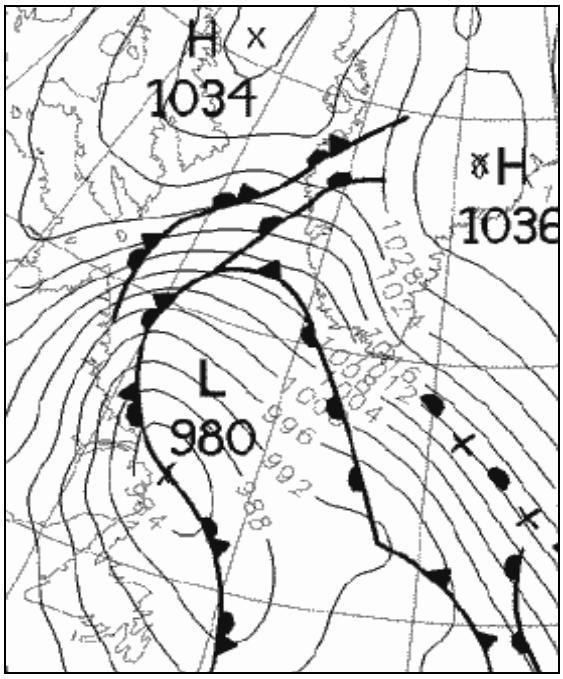

Anomalous winter sea ice backscatter and brightness temperatures

September 2003

Rasmus Tonboe
Søren Andersen
Leif Toudal

ISBN 87-7478-489-7
ISSN 0905-3263 (printed)
ISSN 1399-1949 (online)
Copenhagen 2003

Preface

The Danish Meteorological Institute (DMI) and Technical University of Denmark (TUD) are responsible for investigating methods to better monitor sea ice concentrations in the Arctic using microwave data in the EU funded project Integrated Observing and Modelling of the Arctic Sea ice and Atmosphere (IOMASA). The present report is a DMI and TUD contribution to the IOMASA project.

Sea ice concentration computed using space-borne passive microwave data is biased by atmospheric constituents like cloud liquid water, water vapour and surface wind over open water, but also by changes in the ice surface emissivity. This report is investigating changes in the ice surface emissivity and its impact on sea ice concentration estimates from common ice concentration algorithms relevant for the IOMASA project.

The continuous record since 1999 of Ku-band QuikScat SeaWinds Scatterometer data has opened new opportunities to monitor sea ice scattering properties seasonally and regionally. Ku-band (13GHz) is with respect to wavelength, snow and sea ice scattering mechanisms more closely related to the 19GHz DMSP-SSM/I radiometer channel than the previous long time (1992-2001) scatterometer record by the C-band (5GHz) ERS 1 and 2. Direct correlation between Ku-band backscatter and Tb_{19GHz} is not feasible but forward models reveal common scattering mechanisms related to central snow and ice properties. The scattering problem can therefore be treated with different focus and it is possible to provide a more complete geophysical description of the snow and ice system using both scatterometer and radiometer.

Sea ice surface melt and the resulting change of ice and snow properties significantly influence the radiometer brightness temperature (emissivity) which is used in the computation of sea ice cover concentration. Certain ice concentration algorithms are more sensitive to the melt induced changes than others. The following report takes departure in winter ice surface melt cases and analyse the recorded brightness temperature changes using additional microwave and meteorological data and microwave forward models. Three ice concentration algorithms are tested for low sensitivity to the mentioned ice surface melt and further use in the project.

The weather chart from Bracknell on the front page is showing the pressure systems around southern Greenland December 18th, 2001. Warm air is at this occasion advected into the Baffin Bay region causing ice surface melt. The melt induced metamorphosis of the snow cover gives the first-year ice cover highly anomalous scattering and emissivity in the microwave region.

List of contents

1. Summary

Warm air advection in winter over Arctic sea ice significantly change the snow and ice properties and both the satellite radar backscatter (σ_0) and radiometer brightness temperature (Tb) measurements. Processes are different for first-year ice and multi-year ice, i.e. for first-year ice the weathered foot-print observed by the satellite is permanent and remains for months while multi-year ice satellite measurements are influenced most during the actual event and recover in days or a week. The first- and multi-year ice concentration (IC) computed using the NASA team algorithm for DMSP SSM/I radiometer Tb measurements is depressed by 20% after such events. In comparison, the bootstrap IC algorithm increase by 10% during the event. Radiative transfer model simulations of first-year ice σ_0 and Tb indicate that in particular QuikSCAT SeaWinds (SeaWinds) Ku-band σ_0 measurements are affected by both snow grain size and ice surface roughness increase, Radarsat C-band HH ScanSAR σ_0 measurements are affected by ice surface roughness increase and DMSP SSM/I Tb is mainly influenced by the increased snow grain sizes and ice crusts caused by the temporary warm spell. The multi-year ice σ_0 and Tb are influenced by the wet snow pack during the temporary melt while the polarisation ratio (PR_{19GHz}) and gradient ratio ($GR_{19\text{-}37GHz}$) are changed several days after refreeze. The persistency of the perturbed Tb means that in large areas during significant parts of the winter the computed IC from the radiometer algorithms is biased by up to 20%.

2. Introduction

Warm air spells and temporary ice surface melt over sea ice in the Arctic occur often during autumn and winter (Oct. - Apr.) especially along the ice edge. The events occur weekly on small and intermediate scales (15 000-150 000 km^2) and occasionally also on larger scales (360 000 km^2). The large events can penetrate deep into the central Arctic Ocean. The frequency of occurrence 2000-2002 and size of event (>15 000km^2) is shown for the Arctic in figure 1.

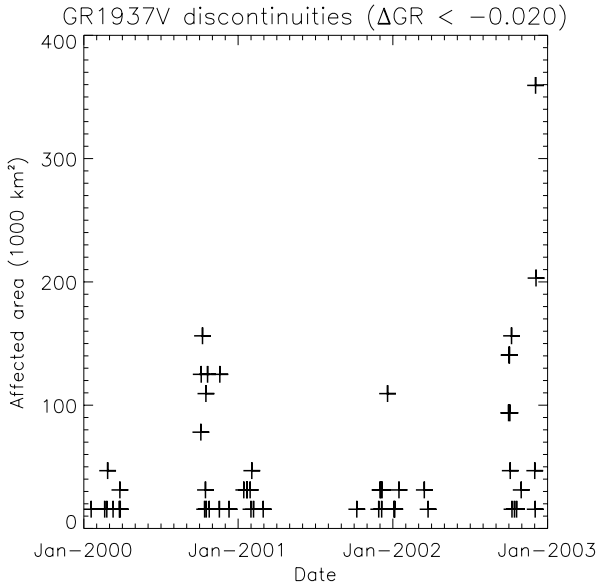

Figure 1. The frequency and size of sea ice surface melt during autumn and winter 2000-2002

The freeze-up after melt (shown in figure 1) is detected by recording cases on a 125km grid when $GR_{19\text{-}37GHz}$ drop by more than 0.02 (selected experimentally) from one day to the next and the bootstrap IC remains >95% in winter. The temporary melt events change the snow and ice properties that are important for σ_0 and Tb. The duration of the events is 1-3 days related to the scale and period of low-pressure weather systems. The periods that we have used in the following study are short (2 weeks) because we study fixed geographical areas and there is no correction for sea ice drift. Anyway, the footprint of the weathered first-year ice remains in Davis Strait ~1 month, in Baffin Bay for ~2 months and Barents Sea ~3 month. The weather-inflicted footprint for multi-year ice is prominent in the satellite data σ_0 and Tb during the actual melt. After refreezing of multi-year ice σ_0 recover to the initial level while e.g. NASA team IC remain depressed below the virtual IC level in multi-year ice for weeks after refreezing. These events potentially corrupt the computation of Arctic winter ice and snow properties in general using microwave data e.g. ice type and IC over significant areas and long periods. Radiometer sea ice concentration algorithms are using typical brightness temperatures when computing the ice concentration i.e. tie-points for ice and water. NASA team is using multi polarisation and frequency brightness temperatures to estimate fractions of first-year ice, multi-year ice and open water within the resolution cell. The computed sea ice concentration is corrupted when the important snow and ice parameters are not typical (Fuhrhop et al., 1997). After temporary melt of first-year ice σ_0 and Tb change to levels typical for multi-year ice. APR however indicate that the scattering characteristics of weathered first-year ice and multi-year ice are different. APR of typical multi-year ice is ~0.17 and first-year ice ~0.23. APR of weathered first year ice is either unchanged or larger (0.23-0.4) than normal first-year ice. In multi-year ice APR does not change significantly after weathering. In the following we analyse warm spells in the waters around Greenland and in Barents Sea us-

ing QuikScat SeaWinds, DMSP SSM/I, Radarsat ScanSAR and meteorological data. The objective is to identify such cases using large scale active and passive microwave satellite observations and to select an ice concentration algorithm which is less sensitive to changes in the snow and ice properties under and after such meteorological events.

Computing sea ice concentration using passive microwave data is the most successful application of geophysical algorithms in sea ice remote sensing. Several algorithms have been proposed see e.g. Steffen et al. (1992). We use in addition to the common NASA team (Cavalieri & Gloersen, 1984) and bootstrap (Comiso, 1986) algorithms the near 90GHz high-frequency algorithm (Svendsen et al., 1987). The near 90GHz algorithm is exploiting the fact that the spatial resolution is better at higher frequency.

2.1 Site and sea ice conditions

The areas of interest are the waters around Greenland and Barents Sea as shown in figure 2. The sea ice types covering these waters can roughly be divided into multi-year and first-year ice. The ice cover in Baffin Bay melts away every summer and the bay is covered by first-year ice November – August (Wadhams, 1986). The waters north of Greenland in the Arctic Ocean are covered by sea ice all year round. The dominating ice type is multi-year ice. Along the east coast of Greenland, a mixture of first-year ice and multi-year ice is drifting from the Arctic Ocean through the Fram and Denmark Straits (Koch, 1945; Wadhams, 1986). Barents Sea is covered by first-year ice but significant amounts of multi-year ice may be advected into these waters mainly by wind forcing (Wadhams, 1981).

Greenland is due to its size and height (Summit about 3200m) significantly affecting the atmospheric flow of the lower troposphere and the air exchange between North and South (Cappelen et al., 2001). In winter, Northern winds dominate along the coasts. The airflow at the 500hPa isobar is important for the track of low-pressure systems. A high pressure at the surface due to cold dense air is a depression in the 500hPa isobar height at about 5km in the atmosphere. The winter situation is characterised by a 500hPa height depression normally situated over Baffin Island, called the Canadian cold vortex or polar vortex. The depth of the polar vortex is coupled to the North Atlantic Oscillation (NAO) index (Thompson & Wallace, 1998). Surface low-pressure systems are formed as waves on the polar front east of USA and Canada at the Gulf Stream margin between cold and warm ocean waters (Cappelen et al. 2001). The low-pressure systems normally follow the 500hPa height contours south of Greenland across Iceland and into the Norwegian Sea. When the polar vortex is weak during negative NAO index, the low-pressure systems are occasionally steered into the Davis Strait and Baffin Bay. These pressure systems are significantly affecting the winter weather situation in Baffin Bay and the West Coast of Greenland with relatively high temperatures and precipitation. During the 1990'ies a positive NAO index is correlated to a situation where the winter situation in west Greenland is predominantly cold and dry and the cyclone track is south of Greenland (Hurell, 1995). A positive NAO is on the other hand correlated to increased cyclone activity in Barents Sea and the Siberian Arctic Ocean (Maslowski et al., 2001). Low pressures travelling directly towards Cape Farewell tend to split into two centres and continue north along the Greenland West and East coasts (Cappelen et al. 2001).

Major cyclones entering the Arctic Ocean in winter (December – February) are concentrated in a triangle between the Greenland Sea, eastern Kara Sea and the North Pole. Maximal occurrence of about three systems is concentrated on Svalbard, northern Novaya Zemlya and the

North Pole. The cyclone systems enter from the Barents and Greenland Seas or across Greenland from Baffin Bay during winter (Serreze & Barry, 1988).

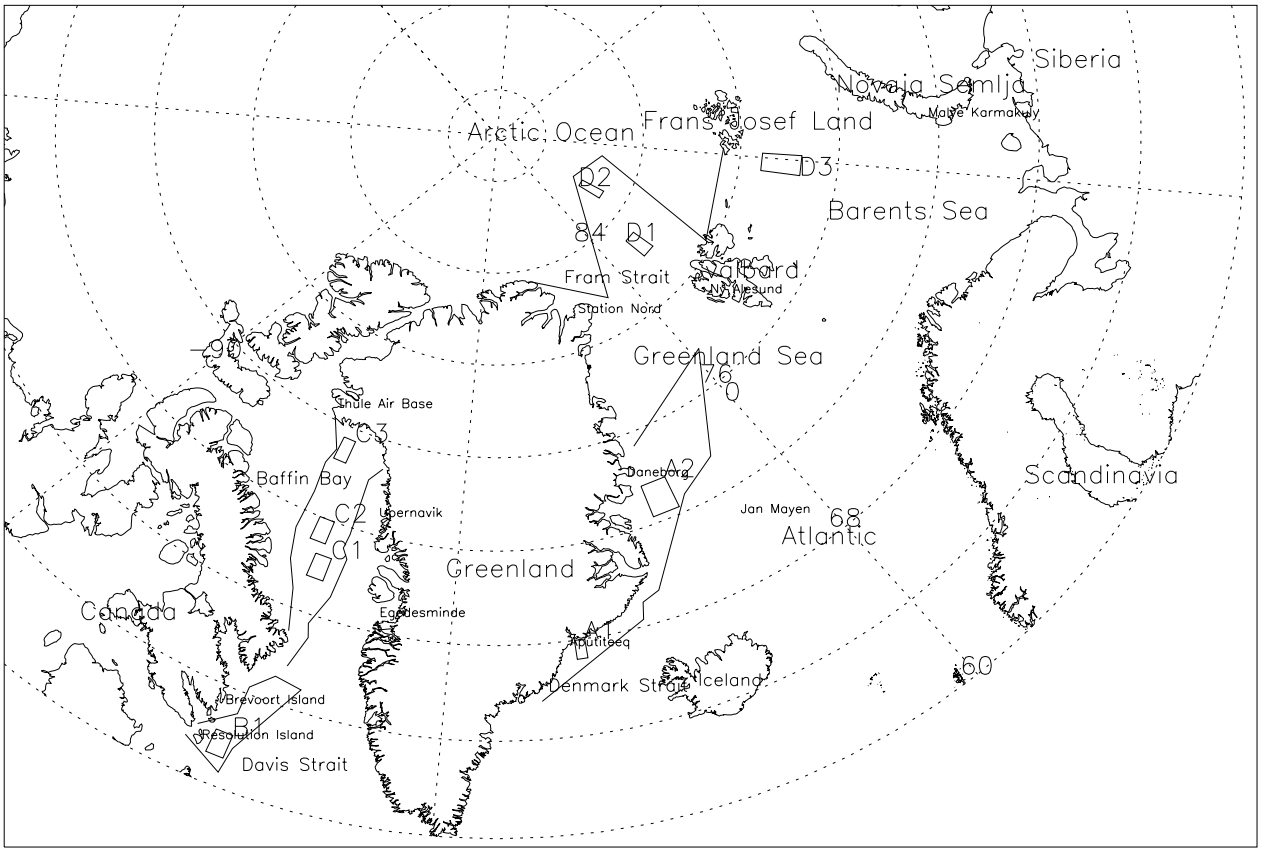

Figure 2. Map of Greenland and Barents Sea.

2.2 Literature background

Several earlier studies describe Arctic snow and ice metamorphism and microwave signature evolution during the annual spring and summer melt (e.g. Garrity, 1992; Barber et al., 1995; Winebrenner et al., 1994; Grenfell & Lohanick, 1985; Livingstone & Drinkwater, 1991; Drinkwater, 1989; Holt & Digby, 1985; Onstott & Gogeneni, 1985; Carsey, 1985; Anderson & Drobot, 2001; Forster et al., 2001). Only few have earlier reported on temporary warm spells during winter in the Antarctic and the Arctic (Drinkwater et al., 1995; Voss, 2002; Liu & Curry, 2003). Conditions during early phase of spring melt are to some extent comparable to the warm spells in winter. The present report analyses the melt events both for multi-year ice, first-year ice and ice type mixtures using Ku-band scatterometer, C-band SAR, multi frequency radiometer and meteorological data in fine temporal resolution (1 - 6 daily satellite passages). The focus is on winter warm spells where the air temperature recover to stable and cold conditions (<-5˚C) after a couple of days melt.

Cold sea ice Tb is in general terms affected by the dielectric properties of snow and ice, the scattering from snow grains and air bubbles in the ice and reflections at layering in the snow and ice (Hallikainen & Winebrenner, 1992). In addition Tb is affected by the actual temperature of the snow and ice and especially at higher frequency (85GHz) atmospheric constituents

like cloud liquid water (Liu & Curry, 2003). The σ_0 is in addition to the ice properties affecting Tb also affected by the ice surface roughness (Hallikainen & Winebrenner, 1992).

2.3 Atmosphere and surface temperature

Increased cloud liquid water and the thermometric surface temperature raise Tb (19, 37 and 85GHz). Tb at 85GHz is raised during the passage of low-pressure frontal systems by 30K while 37GHz may increase by 15K and 19GHz by 8K (Liu & Curry, 2003). Oelke (1997) finds that total water vapour in the atmosphere is decreasing PR_{19GHz}. The decrease is largest for low concentration ice and nearly the same for both multi-year ice and first-year ice types. $GR_{19\text{-}37GHz}$ is increasing and PR_{19GHz} decreasing for increasing cloud liquid water, in particular $GR_{19\text{-}37GHz}$ is increasing for multi-year ice and PR_{19GHz} is decreasing for low concentration ice. Depending on the ice type (multi-year ice or first year ice) and actual ice concentration the NASA TEAM ice concentration algorithm computes IC about 10% higher for increases in cloud liquid water and total water vapour in the atmosphere. The increasing $GR_{19\text{-}37GHz}$ as a consequence of increased cloud liquid water is significantly reducing the multi-year ice concentration computed with the NASA TEAM algorithm (Oelke, 1997).

2.4 Snow metamorphosis

Snow metamorphosis is particularly rapid when the snow is melting (>0˚C). The net result of snow melt, whether the snow is liquid saturated (>14%) or just moist i.e. pendular, is a snow grain size increase (Magagi & Bernier, 2003; Garrity, 1992; Barber et al. 1995; Colbeck, 1982). The grain size growth process in saturated snow is characterised by mass transfer or *cannibalizing* i.e. the larger snow grains grow at the expense of the small grains. The growth process in moist snow is a combination of grain clustering, vapour diffusion and grain surface diffusion (Colbeck, 1982). Barber et al. (1995) indicate that the growth process in the upper-mid portion of the snow pack is due to water vapour diffusion while the lower snow pack just above the ice surface is wet and snow grains grow by grain clustering.

In spring before melt the snow thickness on sea ice is 20-30cm in the Greenland and Barents Seas (Garrity, 1992), ~15cm in the Labrador Sea (Drinkwater, 1989) and 10-15cm for the Arctic sea ice in general (Tucker et al. 1992). The snow pack insulates the ice surface against the cold or warm atmosphere with a heat conduction coefficient of ~0.3 W/mK compared to e.g. ~2.1 W/mK for sea ice (Maykut, 1986). The σ_0 and Tb are both directly affected by the snow properties e.g. liquid water content, grains size, density etc. and indirectly by the thermodynamic control of the snow cover on the ice e.g. ice brine volume (Barber et al., 1995). The relatively thin snow cover in the Arctic Ocean can give large temperature gradients within the snow e.g. during early spring melt, the upper portion temperature of the snow can be ~4˚C higher than the lower portion of the snow (Garrity, 1992) and the other way around when the atmosphere is cold. A strong temperature gradient and the resulting vapour flux forms depth hoar crystals of 2-5mm in diameter at the snow-ice interface or near the snow surface (Garrity, 1992; Amstrong et al., 1993; Colbeck, 1989; Colbeck, 1990). The snow grain size is important for the brightness temperature and the spectral gradient (Tb_{19H}-Tb_{37H}) (Josberger & Mognard, 2002).

The computed snow depth on land using satellite passive microwave snow water equivalent (snow depth) algorithms is problematic in regions with frequent warm spells in winter. This is in particular due to increased scattering by snow grain size enlargement and reflections from internal layering (Künzi et al., 1982; Hallikainen & Jolma, 1986; Mätzler et al., 1982). The snow crystal sizes at mid depth of the spring snow pack are ~1mm in diameter (Garrity,

1992). Normally snow is a microwave absorber rather than a scatterer. However if the grains grow large compared to the wavelength snow become a significant backscatter source (Mätzler et al., 1982). This corresponds to observations in Ku-band σ_0 and Tb at the early stage of melt (Livingstone et al., 1987). For a medium rough first-year ice (σ_{RMS}: 0.0027m, L: 0.02m) with a 15cm snow layer the modelled Ku-band σ_0, the snow dominate 90% at IA 47˚ for grains 0.002m in diameter. When the grains are < 0.00025m the snow layer backscatter is < 15% of the total σ_0. The model is presented in the next section. To illustrate the snow grain size importance for Tb, Mätzler (1987) gives the following approximate relationship between decrease in Tb_{36GHz} [˚] and the depth, d [cm] of an old snow layer with coarse grains: $\Delta Tb_{36GHz} \approx 10d$. The decrease in Tb_{36GHz} is explained by a Rayleigh scattering model where the scattering is proportional to the sixth power of the snow grain radius and the number of scatterers. In general, Tb decreases and σ_0 increases for increasing snow grain size.

The snow may contain free water even for air temperatures below 0˚C (>-5˚C) and ice lenses may form at the early stage of melt in less than 24 hours (Garrity, 1992). Horizontal ice layers in the snow are important for the continued metamorphism of the snow and directly affect the dielectric, scattering and reflection characteristics of the snow (Mätzler, 1987; Colbeck, 1989). The semi-impermeable layers form a barrier for the flux of water vapour, heat and liquid water and depth hoar crystals may form at the surface of such internal ice layers (Colbeck, 1990).

2.5 Sea ice metamorphosis

The brine volume of first-year ice is proportional to the ice permittivity because the permittivity of liquid brine is 2-3 orders of magnitude larger than solid ice. Several investigations e.g. Vant et al. (1978) and Hoekstra & Cappillino (1971) made simple relationships for the (first-year) sea ice permittivity with brine volume as the only variable. However both air bubble inclusions and the shape of the brine pockets are also important for the permittivity of sea ice (Ulaby et al., 1986; Shokr, 1998; Hallikainen & Winebrenner, 1992). Scattering in the ice volume is determined by the number and size of inclusions, in particular air bubbles, and backscattering is in addition affected by the surface roughness (Fung & Eom, 1982). These ice properties described in the following can change after a temporary temperature increase to the sea ice melting point.

A brine surface layer may form through the expulsion of brine from the upper first-year ice sheet, through the melting of the ice surface or through the process of dehydration (Onstott, 1992). The ice surface roughness increase under this process because of the irregular wicking of brine into the snow layer or the formation of frost flowers infiltrated with brine if there is no snow (Ulander et al., 1995; Lohanick & Grenfell, 1986; Barber et al., 1995; Onstott, 1992). The increased roughness has direct impact on σ_0 but a minor influence on Tb. Volume scattering from the ice affecting both σ_0 and Tb is more critically determined by temperature after a surface brine layer formation because it may freeze or thaw around certain temperatures (Onstott, 1992). Salts in brine start sedimenting at particular temperatures e.g. mirabilite ($NaSO_4$ $10H_2O$) at -8.2˚C and hydrohalite (NaCl $2H_2O$) at -22.9˚C. Especially the sedimentation of hydrohalite is related to the total brine volume.

The micro-structure, in particular air bubbles, brine volume and brine inclusion shape of first-year sea ice undergo irreversible changes when the ice temperature increase from cold (<-15˚C) to near melting (-2˚C) (Arcone et al., 1986; Light et al., 2003). The elongated and vertically oriented brine inclusions in columnar first-year ice contain air bubbles. When the ice is heated e.g. from <-15˚C to -2˚C, the brine inclusions and bubbles merge in larger brine tubes.

The merged brine tube shape remain intact after re-cooling (-13˚C) although the diameter is reduced. This temperature driven hysteretic process gives a more anisotropic brine system structure of the ice after re-cooling (Light et al., 2003). Both the dielectric constant permittivity and loss of the ice are reduced by the heating and subsequent cooling (Arcone et al., 1986).

Both σ_0 (>4GHz) and Tb are related to the snow wetness. The dielectric constant of water (ε_{water}>35 below 20GHz) is much higher than dry snow ($\varepsilon_{dry\ snow}$~1.5). The σ_0 gradually decrease and Tb increase for increasing snow wetness (e.g. Stiles & Ulaby, 1980). When the snow is wet, the snow extinction coefficient increase to a degree where the ice volume and surface scattering diminish and σ_0 decrease. Because of reduced scattering in snow and ice Tb increase. This corresponds to observations on sea-ice (Livingstone et al., 1987).

Winebrenner et al., (1994) used C-band VV ERS SAR imagery to analyse the σ_{0VV} decrease from multi-year ice at the onset of melt. C-band multi-year ice scattering is dominated by limited selection of ice properties, i.e. ice volume scattering from air bubbles in ice, rough ice surface scattering and wet snow. C-band σ_{0VV} is not significantly affected by e.g. snow grain size increase, and even if the snow grains had grown during melt this is not reflected in C-band σ_{0VV} (Winebrenner et al., 1994).

3. Radiative transfer models for backscatter and brightness temperature

At moderate and high incidence angles where volume scattering is dominating Ku-band backscatter of sea-ice the intensity is approximately proportional to the scatterer size raised to the sixth power. By doubling the scatterer size the backscatter intensity is magnified 64 times. At the same time the extinction coefficient is increased similarly. The large air bubbles or large snow grains are in other words very important for the backscatter intensity. Areas on the ice floe containing many large bubbles i.e. hummocks and low density snow-ice or large snow grains in metamorphosed snow and depth hoar will dominate the backscatter measurement within the footprint of the radar.

The emissivity of sea ice is reduced for increasing scatterer size as the extinction coefficient increase. The areas on the ice floe there the emissivity is high, i.e. frozen melt-ponds with no or fine grained snow are to some extent complementary to the areas dominating Ku-band backscatter. Simulating both backscatter and emissivity of sea ice using the same ice parameters does therefore not necessarily give results which are comparable to radar and radiometer measurements of the same ice. This mismatch is not expressing a deficiency in the models to simulate measurements, but is simply related to the different mechanisms dictating σ_0 or Tb. The modelling results in the following show that by changing central snow and ice parameters in the models it is anyway possible to simulate both the observed σ_0 and Tb trends.

3.1 Backscatter

The backscatter processes in sea ice can be described using simple radiative transfer backscatter models (Eom & Fung, 1982; Kim et al., 1985; Carlström & Ulander, 1993; Dierking et al., 1999; Livingstone & Drinkwater, 1991; Drinkwater, 1989). The description of the sea ice medium is simplified in the model. The snow grains in the snow layer are modelled as a collection of small spherical fresh ice particles of uniform size distributed in air background. If the snow is wet, the background is a mixture of air and water droplets. The dielectric constant of wet snow is computed using the Debye like formulation given by Hallikainen et al. (1986) and dry snow using Appendix E-6 in Ulaby et al. (1986). Scattering from the snow volume ice particles is computed using Rayleigh scattering theory (Ulaby et al., 1981; Reber et al., 1987). The air/snow interface is characterised by the roughness and the dielectric properties of the snow pack. The scattering from the snow surface is computed using the Integral Equation Method (IEM) for single scattering (Fung, 1994, p.249) and an exponential surface roughness distribution. The ice is modelled as a mixture of fresh ice, brine pockets and air bubbles. The scattering is from the air bubbles in the ice volume and is computed using Rayleigh scattering theory. The dielectric constant of the ice is computed using the Polder Van Santen formulas for dielectric mixtures (Polder & Van Santen, 1946). We follow the recommendations by Shokr (1998), e.g. first-year frazil ice is best modelled as randomly oriented brine needles in pure ice, first-year columnar ice as vertically oriented brine needles in pure ice and multi-year hummock as any shape of air inclusions in pure ice. The ice surface scattering is computed using IEM in C-band and geometric optics (GO) in Ku-band.

In C-band the first-year ice backscatter is dictated by snow-ice interface surface scattering and the snow layer is largely transparent even for large snow grains (>2mm). The essential first-year ice signature can therefore be captured using a surface scattering model for the rough snow-ice interface (Dierking et al., 1997). The C-band multi-year ice model should account

for both ice surface scattering and ice volume scattering (Carlström & Ulander, 1993). Model experiments in both typical first-year and multi-year ice indicate that more backscatter processes are significant for the total backscatter in Ku-band than in C-band (Kim et al., 1985; Fung & Eom, 1982). In particular in Ku-band the snow volume scattering, ice volume scattering and snow-ice interface surface scattering contribute significantly to σ_0 ($\theta>30^\circ$). The Ku-band model has to account for all these scattering mechanisms.

The Rayleigh scattering approximation is valid for scatterers significantly smaller than the wavelength i.e. $|n\chi|<0.5$, where n is the refractive index and χ is the wavenumber, k times the particle radius, r (Ulaby et al. 1981). Mätzler (1987) gives a slightly more relaxed criteria, i.e. $kr<1$. For natural snow and ice the Rayleigh approximation is sufficient in C-band. In Ku-band the Rayleigh approximation is valid for snow grains <0.002 m in diameter using Ulaby et al. (1982) and <0.007 m using the criteria by Mätzler (1987). The former is normally within the range of snow grain size diameters reported in the literature e.g. Baltic snow ~1mm (Dierking et al., 1999), typical Arctic Ocean snow 0.25-0.5mm (Tucker et al., 1992), new snow 0.6-0.8mm, compact snow 0.8-1.1mm, snow-ice interface granular snow 1.7-2.5mm (Barber et al., 1995). However for special types of re-crystallised snow the larger grain are outside the valid range e.g. depth hoar crystals 2-5mm (Garrity, 1992), granular snow above the snow-ice interface 3mm (Drinkwater, 1989) and 2-8mm (Barber et al., 1995). For air bubbles in sea ice the Rayleigh approximation is valid in Ku-band for bubbles about <3.5 mm in diameter. Also here the Rayleigh limit is smaller than the larger bubbles reported in the literature e.g. multi-year hummock 1.6-3.3mm (Onstott, 1992), Baltic first-year ice 0.2-5mm (Dierking et al., 1999), multi-year ice <5mm (Shokr, 1998). We use uniform snow grain and bubble sizes and simulate the backscatter trend approximately within the valid range of the Rayleigh model.

The snow-ice interface is characterised by its surface roughness and the dielectric properties of the snow and ice. The ice surface scattering in Ku-band is computed using the geometric optics GO method for rough surfaces and/or high frequency and an exponentially distributed surface roughness (Fung, 1994). In C-band, we use IEM. The validity of IEM for an ice surface and exponential roughness spectra is: $k^2\sigma L < 1.6\sqrt{\varepsilon_r}$ (Fung, 1994). The valid (RMS) roughness for Ku-band is ~5 times smaller than that for C-band. For GO the valid range is $\sigma\cos(\theta)/\lambda > 0.25$ and $L>\lambda$ (Dierking et al., 1999). Most reported natural ice surface roughness measurements are neither within the valid range of IEM or GO in Ku-band. We have chosen the GO model for Ku-band because the surface scattering is most significant in the range where GO is valid and the ice surface may increase roughness after melt. IEM is suitable in C-band for the lower range of ice surface roughness reported in literature. Figure 3 shows the valid range of different surface models together with surface roughness measurements from the literature. The exponential surface roughness spectrum is better suited for level undeformed ice surfaces while a Gaussian spectrum is better for deformed ice (Livingstone & Drinkwater, 1991).

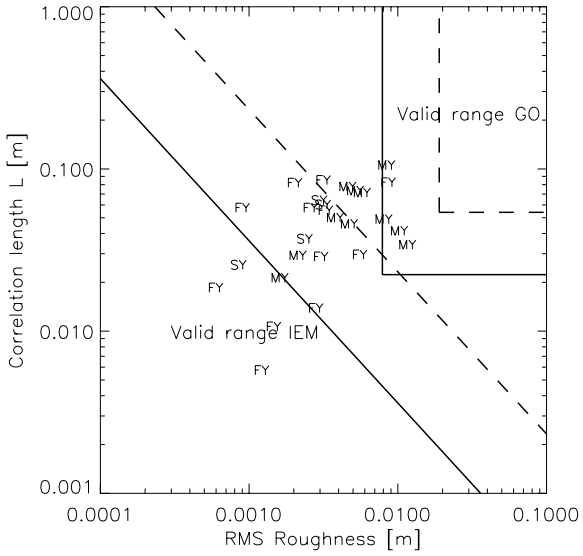

Figure 3. The valid range of IEM and GO given by Fung (1994) and Dierking et al. (1999) together with roughness measurements for natural sea ice reported by Onstott (1992), Carlström & Ulander (1993), Dierking et al. (1999), Nghiem et al. (1995). IEM is valid in the space below the diagonal straight lines in Ku-band (full line) and C-band (dashed line) for an exponential surface. The horizontal and vertical lines delineate the valid space of the GO model for incidence angles at 45°. The dielectric contrast ε_r is 3.15 and the wave number for Ku-band of 280 and C-band 110 is used. FY is first-year ice, MY is multi-year ice, and SY is second-year ice.

If the spacing between scatterers in a media is less than the electromagnetic wavelength, the far-field approximation is no longer valid and the volume scattering coefficient should be corrected for dense scattering medium effects (Kunga et al., 1991; Chuah et al., 1996; Tjuatja et al., 1992; Schanda, 1987; Mätzler, 1987; Fuhrhop et al., 1997). The far field approximation is generally not valid for snow and sea ice in Ku-band (2cm) and C-band (5cm) (Mätzler, 1987). In C-band, this is often neglected because volume scattering is not the dominating scattering mechanism for (first-year) sea ice. In Ku-band, volume scattering is significant. However, a dense scattering medium correction requires detailed knowledge of the distribution of scatterer size and relative position (Chuah et al., 1996; Winebrenner et al., 1992; Fuhrhop et al., 1997). The distribution of the scatterers is not well known and variations in the distribution parameters have a large impact on the computed backscatter and extinction coefficients. We therefore do not apply a correction for the dense media effects and note that earlier studies have simulated Ku-band backscatter measurements from sea ice by similar models without dense media correction (Kim et al., 1985; Fung & Eom, 1982).

The following equation describes the total backscatter from an ice surface covered by snow. The ice has two layers and there is water underneath (water is not shown in equation 1 and is insignificant for the backscattering). Interaction between surface and volume scattering is neglected as in Carlström & Ulander (1993) i.e.

$$\sigma^0(\theta) = \sigma^0_{ss}(\theta) + T^2_{as}(\theta)(\sigma^0_{sv}(\theta') + \frac{1}{L^2_s(\theta')}(\sigma^0_{i1s}(\theta') + T^2_{si1}(\sigma^0_{i1v}(\theta'') + \frac{1}{L^2_{i1}(\theta'')}(\sigma^0_{i2s} + T^2_{i1i2}\sigma^0_{i2v}(\theta''')))))$$

(Eq. 1)

σ^0 is the backscatter coefficient, T is the transmission coefficient; L is the loss factor, the subscript ss is for snow surface, sv snow volume, as air-snow, s snow, is ice surface, si snow-ice, iv ice volume.

3.2 Emissivity

Important radiative processes in a homogeneous snow layer can be described using simple radiative models (Ulaby & Stiles, 1980; Mätzler, 1987). The dielectric properties of the snow are determined mainly by the density and wetness (Ulaby et al., 1986). The dielectric constant of snow is affecting the reflection and transmission coefficients and the absorption coefficient. Scattering in the snow pack becomes important for large snow grains or high frequency (Mätzler, 1987). In order to illustrate these radiative processes and the physical parameters dictating the emissivity of snow we have applied a simple 2-layer model for a snow layer described in Ulaby et al. (1982) p. 243 i.e.

$$T_B(\theta_1; p) = \frac{1-\Gamma_1}{1-\frac{\Gamma_1\Gamma_2}{L_2^2}}\left[(1+\frac{\Gamma_2}{L_2})(1-\frac{1}{L_2})(1-a)T_2 + \frac{1-\Gamma_2}{L_2}T_{B3}\right] \quad \text{(Eq. 2)}$$

The subscripts in equation 2 refer to the layer number where 1 is air, 2 is snow and 3 is the infinite half-space of ice here given a constant brightness temperature, T_{B3}. Γ is the rough surface reflectivity (Ulaby et al. 1981) i.e. $\Gamma_s(\theta; p) = \Gamma^{sp}(\theta; p)e^{-h'\cos^2\theta}$, where Γ^{sp} is the specular surface reflectivity and h' an effective roughness parameter. The dielectric constant of the wet snow layer is computed using the Debye-like formulation in Hallikainen et al. (1986). For dry snow the real part is computed using a polynomial approximation and the imaginary part using a Polder van Santen formulation both given in appendix E-6 in Ulaby et al. (1986). Scattering is computed using the Rayleigh scattering (Mätzler, 1987; Reber et al., 1987).

The microwave model, MWMOD, is a combined atmosphere, ocean and sea-ice radiometer model. The model is using many layer strong fluctuation theory (MLSFT) to model the emissivity or Tb of sea ice. The sea ice model theory is presented in Winebrenner et al. (1992) and applied in Fuhrhop et al. (1998) and Johnson & Heygster (2000). MLSFT is a volume scattering model and does not account for surface scattering effects. The influence of surface scattering for Tb is assumed to be small for most ice types (Fuhrhop et al. 1998).The model Tb is dictated by volume scattering for electrically dense scatters and coherent reflections between layers with dielectric contrast (Stogryn, 1986; Winebrenner et al., 1992). Details are given in the references above. The advantage using this model compared to the simple model presented above is that it treats dense scattering medium effects from non-spherical scatterers. The drawbacks are coherent interference effects of radiation from the horizontal plane layers, underestimation of scattering especially at high frequency (≥37GHz) and the initialisation requires specialised knowledge of the size and spatial distribution, shape and orientation of scatterers (Fuhrhop et al., 1998). It further turned out that it was difficult to simulate a realistic emissivity of multi-year ice using typical ice and snow parameters from the literature.

The coherent interference between the horizontal layers of ice and snow simulated in MWMOD can have a significant impact on the computed Tb (Johnson & Heygster, 2000). Johnson & Heygster (2000) computed the brightness temperature of a forming fresh ice cover and found that as the ice grew from about 0.10m to 0.20m the modelled Tb_{37H} decreased from 260K to 120K. When the ice continued its growth to 0.3-0.4m, Tb_{37H} increased again to 260K. Even though these interference effects are real on small scales with a very smooth and uniformly layered media, it never occurs on large scales like the SSM/I footprint (Johnson & Heygster, 2000). Considering these large oscillations in MWMOD Tb which are a function of frequency, layer spacing, dielectric properties and thickness it is unrealistic to compute the IC sensitivity to snow and ice parameters using different algorithms. Combined radiative transfer strong fluctuation theory (CSFT) was later developed to deal with the oscillations in strong

fluctuation theory (Johnsen & Heygster, 2000). CSFT has not been tested in this report. In order to study trends in Tb as a function of central snow parameters e.g. grain size and liquid water content we have in addition to MWMOD used the simple non-coherent 2-layer radiative transfer model presented above.

3.3 Ice properties – model input

The following snow and ice properties are used for initialising both the backscatter and emissivity models.

3.3.1 Snow

The snow properties are identical on both first- and multi-year ice. *Roughness*: RMS surface height 0.0028m and correlation length 0.02 (Nghiem et al., 1995). *Density* is 200 kg/m^3 (Nghiem et al., 1995). *Grain radii* is 0.00025m (Tucker et al., 1992). *Depth* is 0.13m (Tucker et al., 1992).

3.3.2 Multi-year and first-year ice

The Roughness is for first-year ice: RMS surface height 0.005 and correlation length 0.028 (Onstott, 1992). Multi year ice RMS surface height 0.01m and correlation length 0.032 (Onstott, 1992). *Density* of first year ice is 900kg/m^3 (Shokr, 1999). Multi year ice has a density of 750kg/m^3 for the upper 0.12m and 900kg/m^3 further down (Carlström & Ulander, 1993). *Salinity* of first-year ice in the upper layer is 7ppt and multi-year ice 0.1ppt. Further down the salinities are 7ppt and 1.5ppt respectively. *Air bubble radii* of first-year ice is 0.0005m and multi year ice 0.0017m (Shokr, 1999). *Brine pocket dimensions and orientation* (ref). *Total ice thickness* of the first-year ice is 1m and multi-year ice 2m. *The temperature profile* is calculated using an air temperature of -20C and a uniform temperature gradient in snow and ice and thermal conductivities of 0.3WK/m and 2.1WK/m respectively. Under simulations of the liquid water content in the snow, both the snow and ice temperature are at the melting point.

4. Data and data processing

QuikScat Seawinds, DMSP-SSM/I and Radarsat ScanSAR satellite data and the HIRLAM numerical weather prediction model data are used to analyse the warm air events and the resulting snow and ice cover changes.

4.1 Radarsat

The polar orbiting RADARSAT-1 satellite has a SAR onboard operating in C-band at horizontal linear polarisation (HH). The SAR is capable of operating in different modes, both SAR and ScanSAR, at different spatial resolutions between 8-100m and swath widths from 50- 500km. The ScanSAR wide mode gives widest possible swath covering incidence angles from 17˚-49˚ equivalent to ~500km on the ground (RADARSAT data product specifications, 2000). The spatial resolution in this mode is ~100m and the radiometric accuracy is +/- 1.35dB (Srivastava et al., 1999).

Four RADARSAT ScanSAR wide scenes in Baffin Bay cover C1 before and after the warm spell Dec. 20th 2001. The scene details are listed in table 1. These data were calibrated using a procedure described in Sheperd (1998) and geo-referenced using the operational software at DMI.

Date-time	Scene centre coordinates	Comment
Dec. 5th 2001, 21.06 UTC	67˚ 31'N 56˚ 18'W	Cover C1 before event
Dec. 12th 2001, 21.02 UTC	69˚ 00'N 56˚ 17'W	Cover C1 before event
Dec. 22nd 2001, 21.11 UTC	71˚ 02'N 58˚ 57'W	Cover C1 during/after event
Dec. 26th 2001, 20.54 UTC	70˚ 46'N 55˚ 33'W	Cover C1 after event

Table 1. Dates and positions of Radarsat ScanSAR wide scenes.

4.2 QuikScat-SeaWinds

The SeaWinds instrument onboard the QuikScat satellite is a Ku-band (13.4GHz) pencil beam scatterometer using a rotating dish antenna with two spot beams that sweep in a circular pattern. The outer beam is transmitting and receiving at vertical polarisation (VV) with a constant incidence angle of 55˚. The inner beam is transmitting and receiving at horizontal polarisation (HH) at 47˚. The swath width of the outer VV beam is ~1800 km and the inner HH beam is ~1400 km (Leidner et al., 2000). At high latitudes (>55˚) the daily coverage is complete for both polarizations. Dependent on latitude QuikScat SeaWinds covers each sample area with 1-6 passes a day. Backscatter measurements are extracted from each swath if there are more than 2 data points within the sample area. Acquisition time, mean and standard deviation of the measured backscatter are computed for σ_{0HH} and σ_{0VV} and the active (microwave) polarisation ratio (APR) defined as the difference over the sum of σ_{0HH} and σ_{0VV} i.e.

$$APR = \frac{\sigma_{0HH} - \sigma_{0VV}}{\sigma_{0HH} + \sigma_{0VV}} \qquad \text{(Eq. 4)}$$

The standard deviation for both multi-year and first-year ice areas is nearly constant before and after the melt ±2dB for σ_{0HH} and ±0.1 for APR. The absolute level of σ_{0VV} is ~2dB lower than σ_{0HH} the variations are nearly the same. We only show and refer to σ_{0HH} in the following.

4.3 DMSP-SSM/I

The Special Sensor Microwave/Imager (SSM/I) on board the Defence Meteorological Satellite Program (DMSP) satellite is a total power radiometer operating at dual polarisations

(horizontal, H and vertical, V), and multi frequency (19GHz, 37GHz, and 85GHz, and at vertical polarisation in 22GHz). The conical scan covers a 1400km wide swath on the ground at constant incidence angle of 53.1˚ (Hollinger et al., 1990). Mean and standard deviation of the measured brightness temperature is computed in each area for every swath, similar to the processing of scatterometer data. The many frequencies and dual polarisation allows the computation of both gradient and polarisation ratios i.e.

$$PR_{fa} = \frac{Tb_{fa,V} - Tb_{fa,H}}{Tb_{fa,V} + Tb_{fa,H}}$$

$$GR_{fa-fb,P} = \frac{Tb_{fa,P} - Tb_{fb,P}}{Tb_{fa,P} + Tb_{fb,P}} \quad \text{(Eq. 5a \& 5b)}$$

In equation 5a and 5b Tb is the brightness temperature, the subscripts fa is e.g. 19GHz frequency and fb 37GHz. P indicate the polarisation H and V i.e. horizontal and vertical polarisations respectively. In the following we compute the gradient ration using the vertical polarisation. The radiometer Tb is used as input to compute the sea ice cover concentration with the following three algorithms: 1) the NASA TEAM algorithm using polarisation and gradient ratios of Tb_{19V}, Tb_{19H} and Tb_{37V} is described in Cavalieri & Gloersen (1984), 2) the bootstrap algorithm in frequency mode using Tb_{19V} and Tb_{37V} described in Comiso (1986), and 3) the near 90GHz algorithm using the difference between Tb_{85V} and Tb_{85H} described in Svendsen et al. (1987), hereafter just referred to as the near 90GHz algorithm. Comiso et al. (1997) describe 1 and 2 in detail.

4.4 HIRLAM

The high resolution limited area model (HIRLAM) is a mesoscale atmospheric model operated at DMI for analysis and forecast in the weather service. It covers Greenland, the North Atlantic and Europe with different resolutions, from 0.05˚-0.45˚, and uses the global European Center for Medium Range Weather Forecast (ECWMF) model for lateral boundary conditions. We use the model set-up for Greenland with a horizontal resolution of 0.45˚. The analysis is done every six hours using the optimum interpolation method, a statistical procedure to minimize differences between observations and first guess from the model (Sass et al., 2002). The model analysis is checked against measurements from the meteorological stations on land and Bracknell and DMI weather charts to investigate the regional weather situation during the ice surface melt events.

4.5 Melt locations

The locations and warm air event dates summarized in table 2.

Location	Event date Time period	Satellite data sample area	Met. Station	Met. Station Location
A1 Denmark Strait A2 Greenland Sea	Feb. 1st 2001 Day 25-40	30.7-31.8W, 67.2-68.0N 15.2-18.9W, 72.3-73.7N	Aputiteeq Daneborg Jan Mayen	32.3W, 67.8N 20.2W, 74.3N 8.7W, 70.9N
B1 Davis Strait	Mar. 1st 2001 Day 55-70	62.5-64.0W, 61.2-62.2N	Resolution Island Brevoort Island	64.7W, 61.6N 64.2W, 63.3N
C1 Baffin Bay South C2 Baffin Bay mid C3 Baffin Bay North	Dec. 20th 2001 Day 350-365	60.2-62.2W, 69.5-70.5N 61.6-63.6W, 71.0-72.0N 63.5-65.5W, 74.5-75.5N	Aasiaat Upernavik Thule Air Base	52.9W, 68.7N 56.2W, 72.8N 68.8W, 76.5N
D1 Arctic Ocean S. D2 Arctic Ocean N. D3 Barents Sea	Dec. 6th 2002 Day 335-350	9.0-13.0E, 82.0-83.0N 17.0-21.0E, 85.0-86.0N 42.1-46.1E, 77.5-77.1N	Station Nord Ny Ålesund Malye Karmakuly	16.7W, 81.6N 11.9E, 78.9N 52.7E, 72.4N

Table 2. Warm air event dates and locations.

5. Results from four weathered regions

Four cases used for analysing the changes in brightness temperature and backscatter when winter multi-year- and first-year- snow and ice properties are changed during temporary melt events. First the four cases are described separately then the areas dominated by first-year ice and multi-year ice are compared. The warm air advection is driven by low-pressure systems or combinations of high and low pressure systems.

5.1 Denmark Strait

February 1st 2001 the temperature in Denmark Strait and the Greenland Sea rise from ~-5˚C to ~1˚C and then drop to ~-10˚C ~3days later. The temperature records from the weather stations in Daneborg, on Jan Mayen and in Aputiteeq are shown in figure 4. A deep low-pressure (957 Hpa) East of Cape Farewell (45˚W, 60˚N) controls the warm air advection. The temporary air temperature increase is reflected in the backscatter and brightness temperature in A1 are shown in figures 5 and 10 and A2 in figures 6 and 14. In A1 the SeaWinds backscatter drop from ~-10dB before, to ~-15dB during the melting, and then increase to ~-8dB after the re-freezing. The brightness temperature increase temporarily during melting and drop again after refreeze to a level below the initial level. The brightness temperature changes are greater in 37GHz and 85GHz than in 19GHz. PR_{19GHz} shown in figure 7 drop during refreeze from 0.05 to 0.03. $GR_{19\text{-}37GHz}$ in figure 8 drop at refreeze from a typical first-year ice value around 0 to a typical multi-year ice value of -0.07. During 10 days after refreeze $GR_{19\text{-}37GHz}$ recover to the initial level. All bootstrap, NASA team and near 90GHz ice concentration algorithms shown in figure 9 are significantly affected by the melt. Both bootstrap and NASA team IC increase from 85 before melt to 100% during refreeze and near 90GHz IC increase from 80-85 to 110% during the peak of melt. After refreeze the bootstrap, NASA team and near 90GHz IC algorithm concentration estimates stabilize at 80, 90 and 100% respectively. In A2 the back-scatter drop from -10dB to -13dB during the melt and then recover to the initial level after the refreezing shown in figure 6. In both areas APR drop from 0.15 to 0.11 during the melt and then recover to the initial level after the refreezing. The approximate area influenced most by the backscatter increase is delineated with the hand-drawn contours shown in Figure 2. The meteorological and satellite parameters in areas A1 and A2 are shown in figures 4-14.

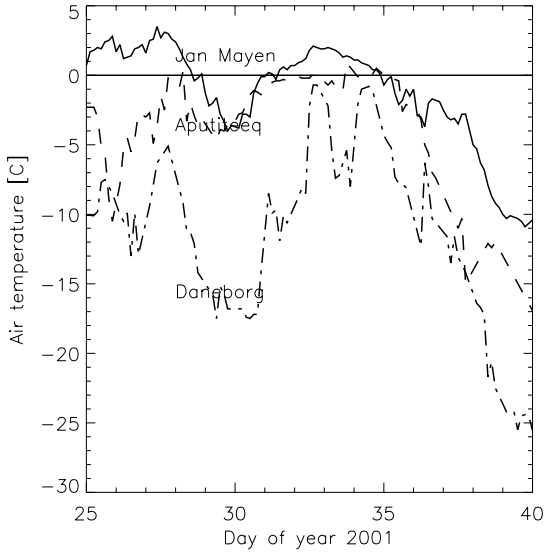

Figure 4. Air temperature [˚C] from meteorological land stations in West Greenland and on Jan Mayen. Records from Aputiteeq, Daneborg and Jan Mayen.

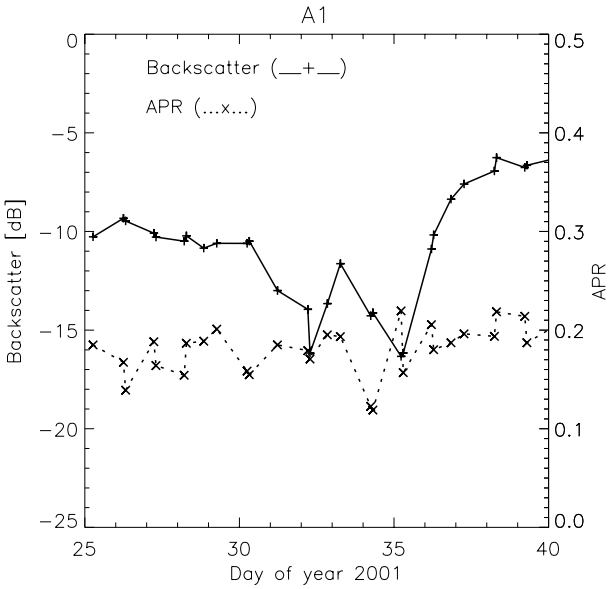

Figure 5. QuikScat SeaWinds HH-backscatter and APR from Denmark Strait, Feb. 1st 2001, day of year 25-40.

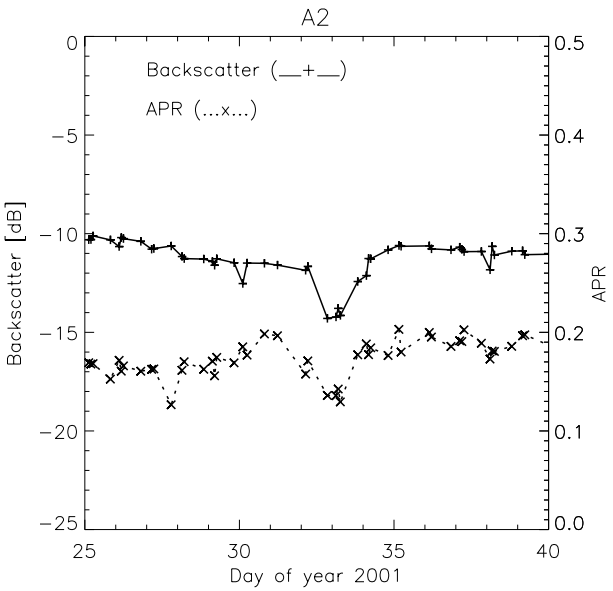

Figure 6. QuikScat SeaWinds HH-backscatter and APR from Greenland Sea, Feb. 1st 2001, day of year 25-40.

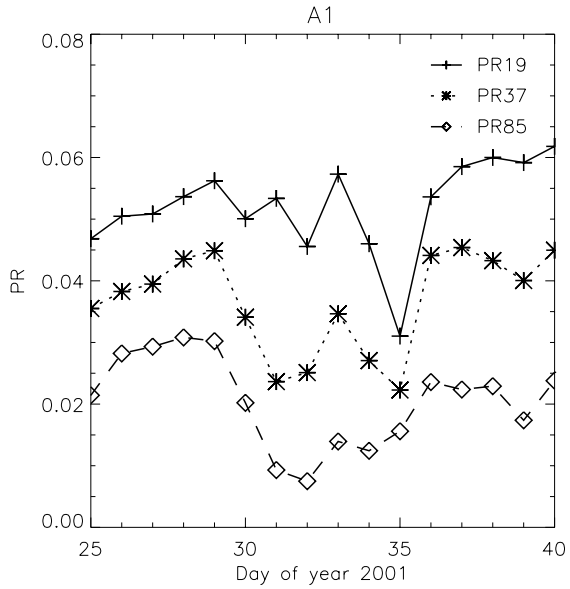

Figure 7. DMSP-SSM/I polarisation ratio evolution in A1.

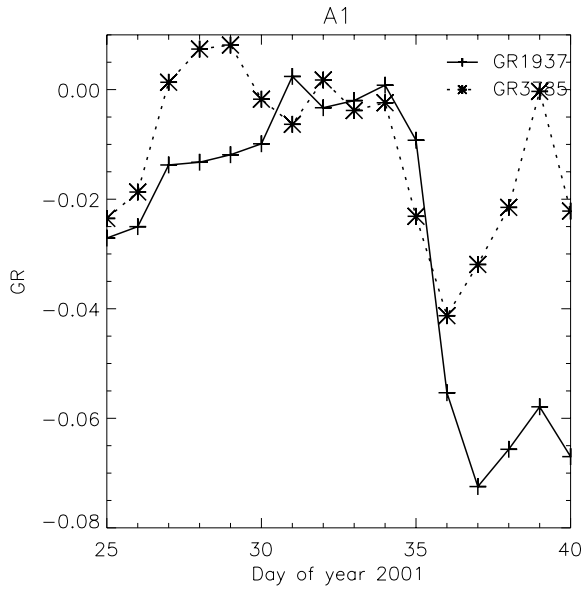

Figure 8. DMSP-SSM/I gradient ratio evolution in A1.

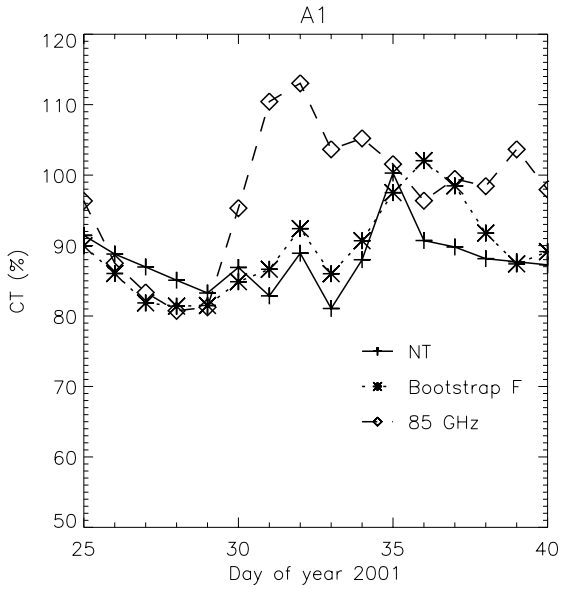

Figure 9. DMSP-SSM/I ice concentration in A1 using the NASA team, bootstrap and near 90GHz algorithms.

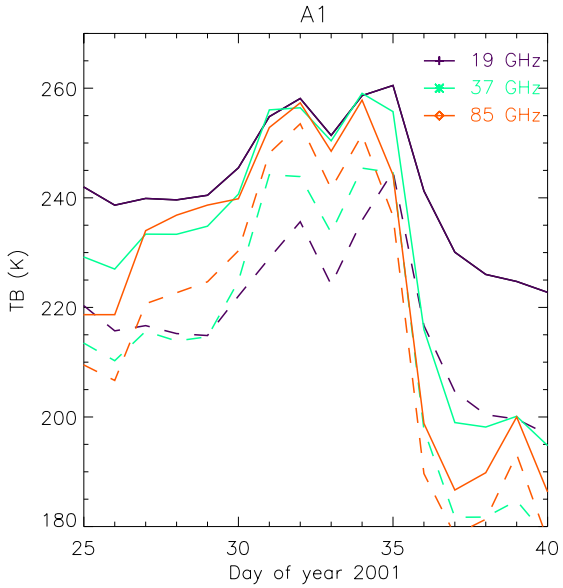

Figure 10. DMSP-SSM/I brightness temperature evolution in A1. Vertically polarised channels with full line, horizontally polarised with dashed line.

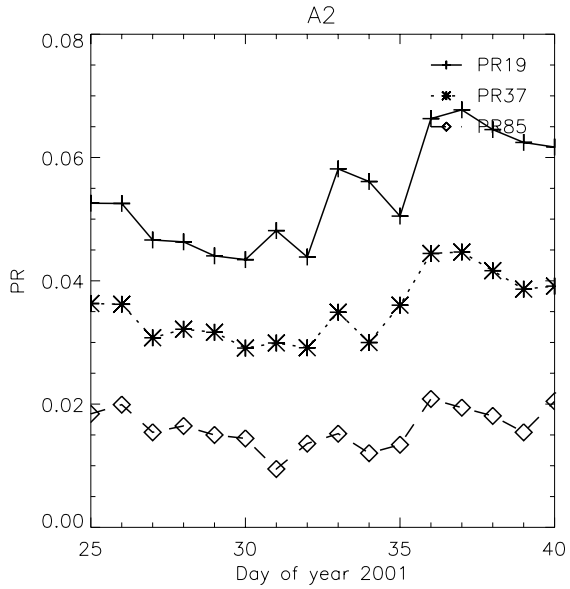

Figure 11. DMSP-SSM/I polarisation ratio in A2.

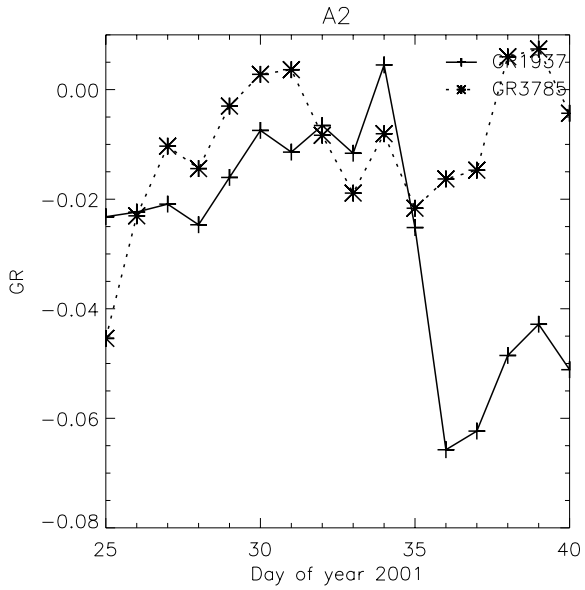

Figure 12. DMSP-SSM/I gradient ratio in A2.

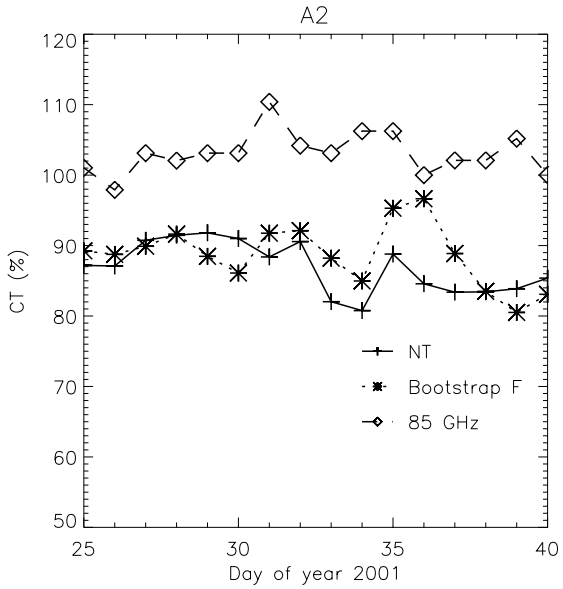

Figure 13. DMSP-SSM/I ice concentration in A2 using NASA team, bootstrap and near 90GHz algorithms.

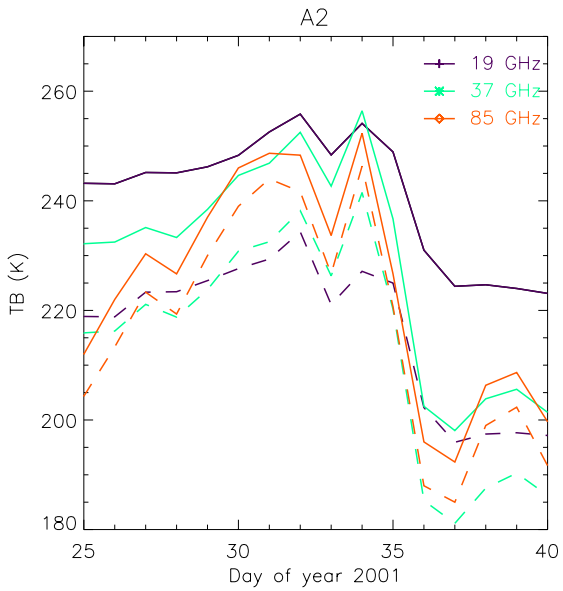

Figure 14 DMSP-SSM/I brightness temperature in A2. Vertically polarised channels with full line, horizontally polarised with dashed line.

5.2 Davis Strait

On March 1st 2001 the air temperature at Resolution Island in Davis Strait shown in figure 15 increase from below -10˚C to ~0˚C and after ~2 days it decrease again to ~-15˚C. The warm air advection is associated with a low pressure system over New-Foundland (57˚W, 50˚N). The temporary air temperature increase is reflected in the backscatter and brightness temperature shown in figures 16 and 20. The SeaWinds σ_0 increase during the melt from about -15dB to -10dB (figure 16). APR shown in figure 16 is unaffected by the backscatter increase. Tb_{19GHz}, Tb_{37GHz} and Tb_{85GHz} in figure 20 decrease by 20K, 40K and 40K respectively at refreeze. $GR_{19\text{-}37GHz}$ in figure 18 decrease during melt from 0 to -0.04 at refreeze. PR_{19GHz} in figure 17 increase from 0.03 to 0.05-0.06. During the melt phase and at refreeze bootstrap IC varies ~5%, NASA team IC ~10% and near 90GHz IC also ~10% (figure 19). Before melting

the 3 algorithms compute the same IC within ~5%, after within ~15%. The meteorological and satellite parameters are shown in figures 15-20.

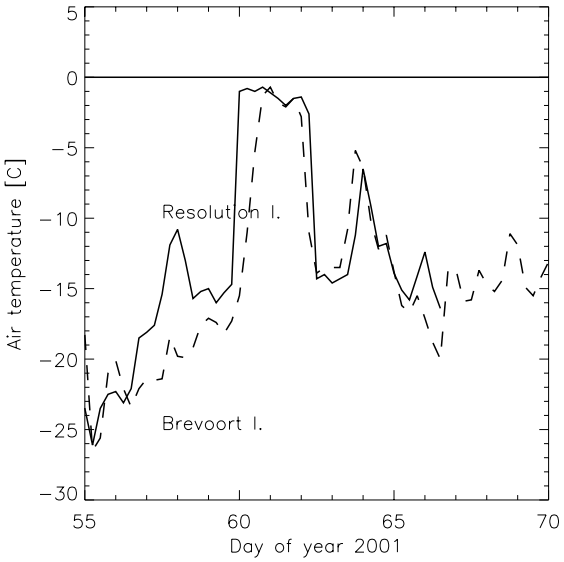

Figure 15. Air temperature [˚C] from meteorological land stations in West Davis Strait. Records from Brevoort Island and Resolution Island.

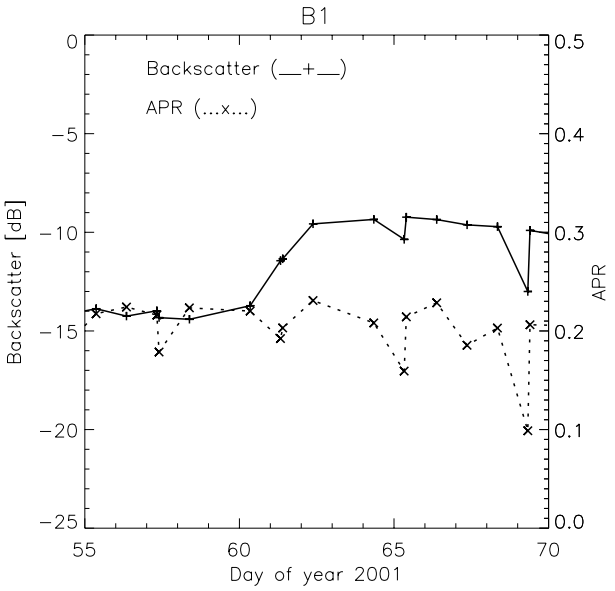

Figure 16. QuikScat SeaWinds measurements from the Davis Strait, Mar 1st 2001, day of year 55-70.

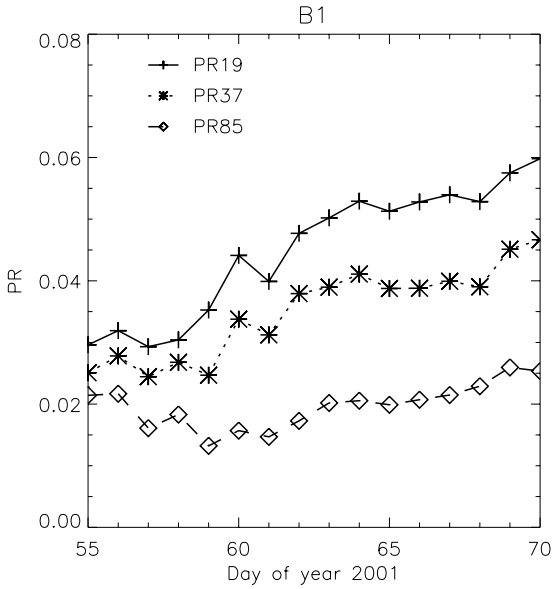

Figure 17. DMSP-SSM/I polarisation ratio in B1.

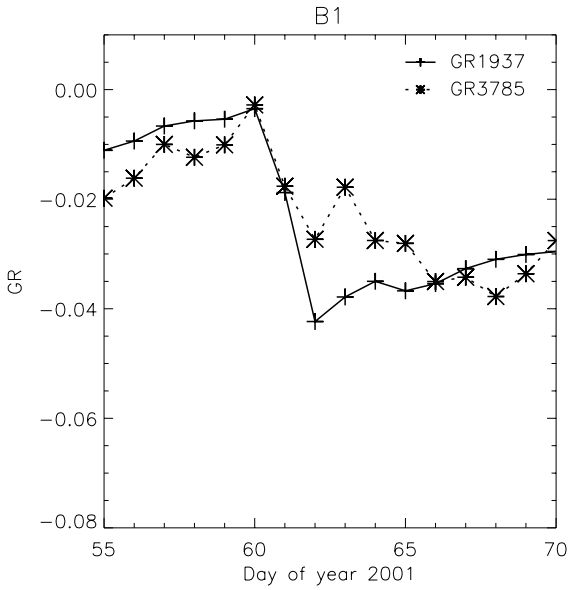

Figure 18. DMSP-SSM/I gradient ratio in B1.

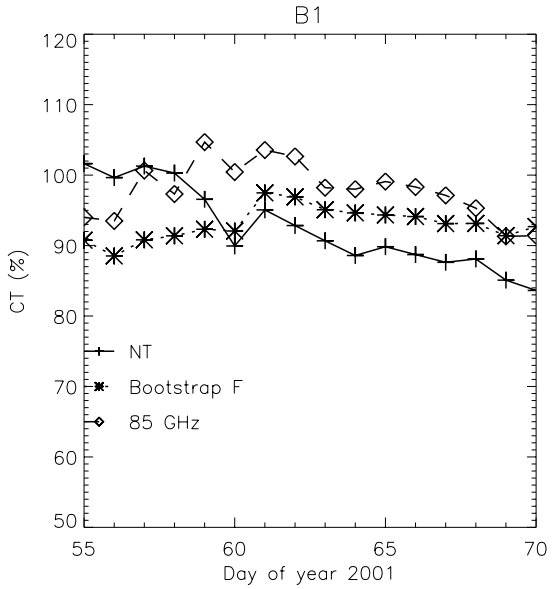

Figure 19. DMSP-SSM/I ice concentration in B1 using NASA team, bootstrap and near 90GHz algorithms.

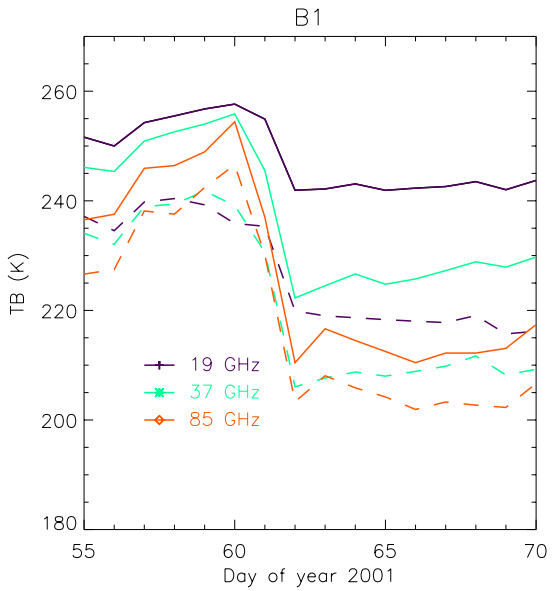

Figure 20. DMSP-SSM/I brightness temperature in B1.

5.3 Baffin Bay

December 20th 2001 the temperature increase from between -30 and -10˚C to above 0˚C in East Baffin Bay. The temperature record from the three meteorological stations on land from south to north Egedesminde, Upernavik and Thule Air Base are shown in figure 21. When the temperature decline again to freezing between -20 and -5˚C 1-3 days after the melt onset the backscatter level has increased from ~-18dB to ~-9dB as shown in figures 22-24. The warm Atlantic air is advected into the bay region by a low pressure over New-Foundland (980Hpa) and a high pressure over South-East Greenland (1032Hpa). The mean backscatter increase is greater in C3 than in C1. APR is shown in figures 22-24. In C1, APR remain at a nearly constant level (0.2-0.25) before, under and after the event. In C2 and in particular C3 the evolution of APR is different than in C1. Before the event, the APR level in C3 is 0.2-0.25. During the warm period APR, drop to 0.0-0.1. After refreezing the APR, level stabilizes above the

initial level (0.3-0.4). The brightness temperature shown in figures 28,32 and 36 increase 10-20K during melt and then the decrease 10-60K below the initial level at refreeze. The changes are larger for 37 and 85GHz than for 19GHz and larger for C3 than C1. $GR_{19\text{-}37GHz}$ shown in figures 26, 30 and 34 decrease during melt from 0 to between -0.025 and -0.07 at refreeze. The bootstrap IC shown in figures 27, 31 and 35 is stable during the melt event in C1 and C2 but in C3 it increase by 10% at refreeze. In all areas NASA team decrease by ~15% at melt onset. near 90GHz IC increase during melt and drop at refreeze.

The meteorological and satellite parameters C1, C2 and C3 in Baffin Bay are shown in figures 21-36.

In two Radarsat ScanSAR scenes covering C1 (December 22nd and 26th 2001) it is possible to identify the same ice floes and the ice drift is estimated. The ice drift is 8-30km south during the 4 days, fastest closer to the ice edge.

Three Radarsat ScanSAR scenes covering C1 on December 16th, 22nd and 26th, 2001 were classified into pixels of ice and water using a neural network classification procedure in order to investigate trends in the ice concentration. The classification procedure is decribed in detail in Karleschke & Bochert (1999). In the area covered by all three scenes, the ice concentration was on 16th, 22nd and 26th, 2001 computed to 94%, 99%, and 98% respectively.

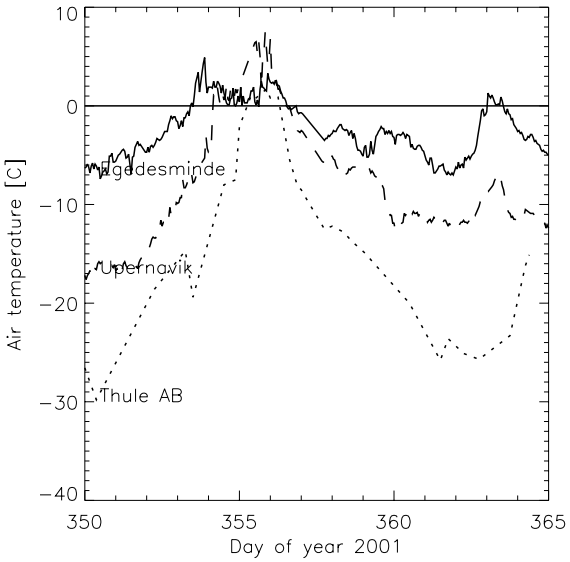

Figure 21. Air temperature [˚C] from meteorological land stations on the Greenland West Coast. Records from Thule Air Base, Upernavik and Egedesminde.

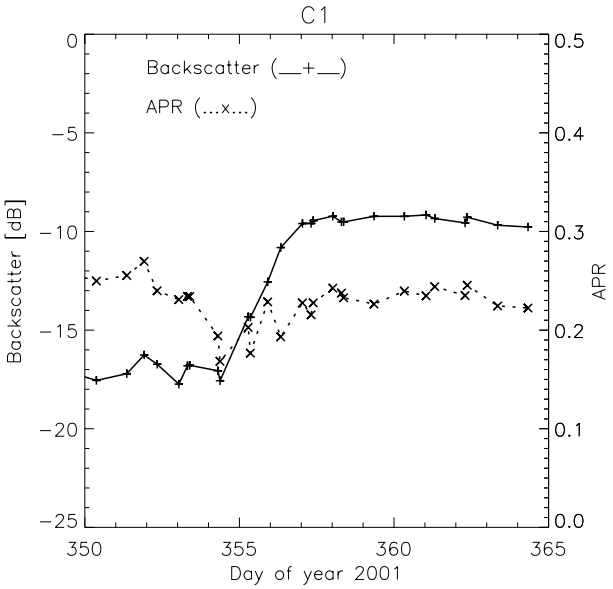

Figure 22. QuikScat SeaWinds HH-backscatter and APR in C1.

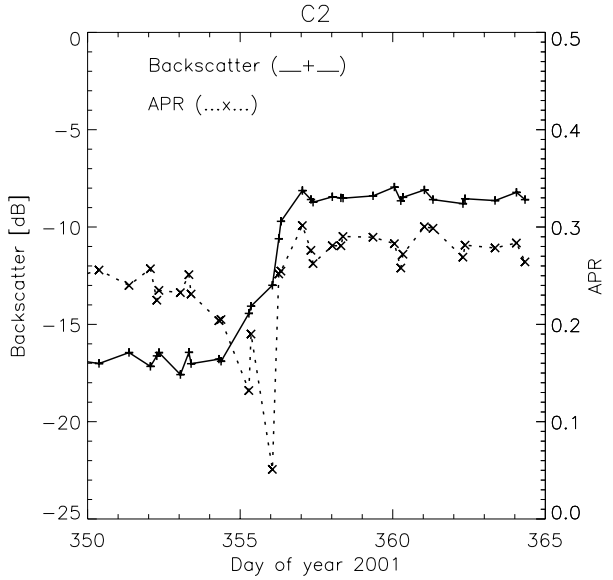

Figure 23. QuikScat SeaWinds HH-backscatter and APR in C2.

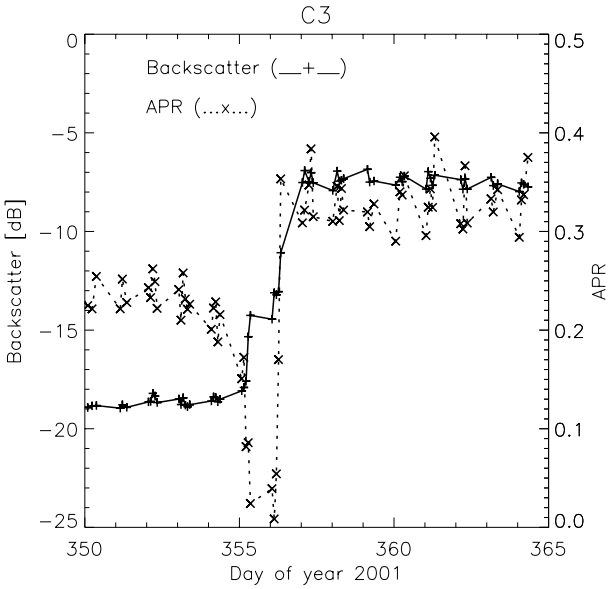

Figure 24. QuikScat SeaWinds HH- backscatter and APR in C3.

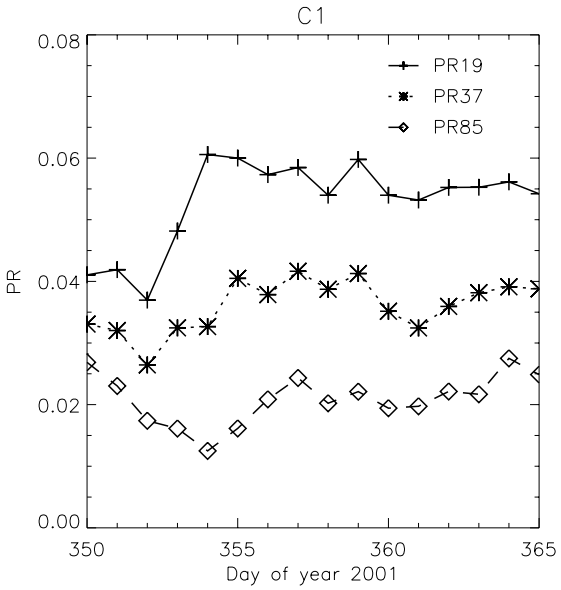

Figure 25. DMSP-SSM/I polarisation ratio in C1.

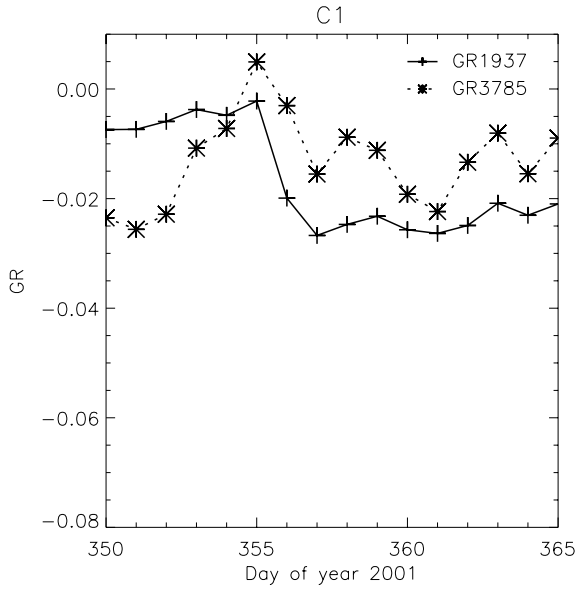

Figure 26. DMSP-SSM/I gradient ratio in C1.

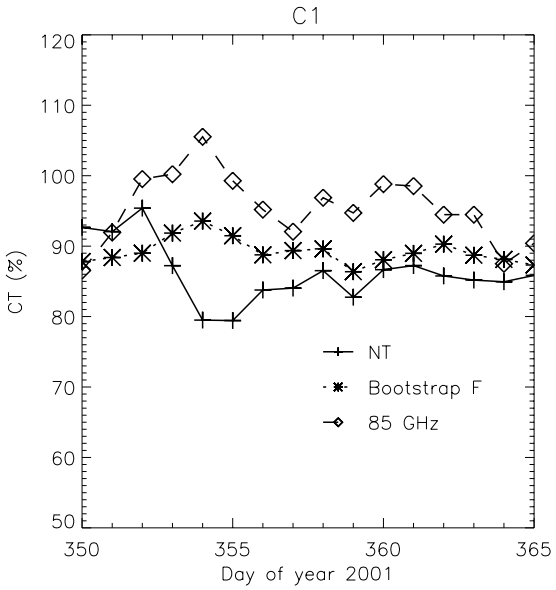

Figure 27. DMSP-SSM/I ice concentration in C1 using the NASA team, bootstrap and near 90GHz algorithms.

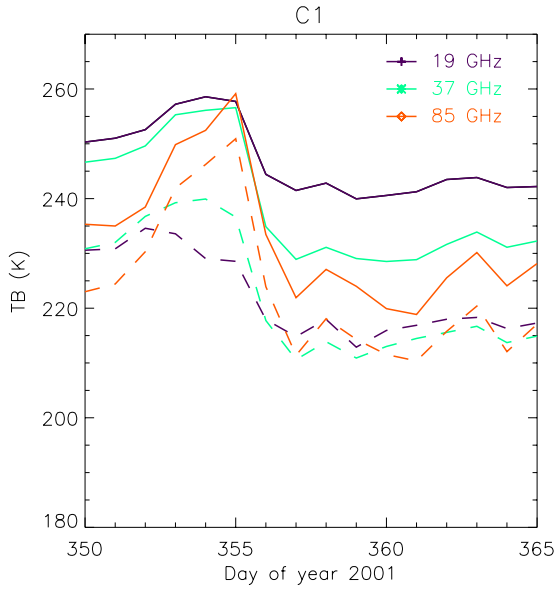

Figure 28. DMSP SSM/I brightness temperatures in C1. Vertical(------), Horizontal(- - -).

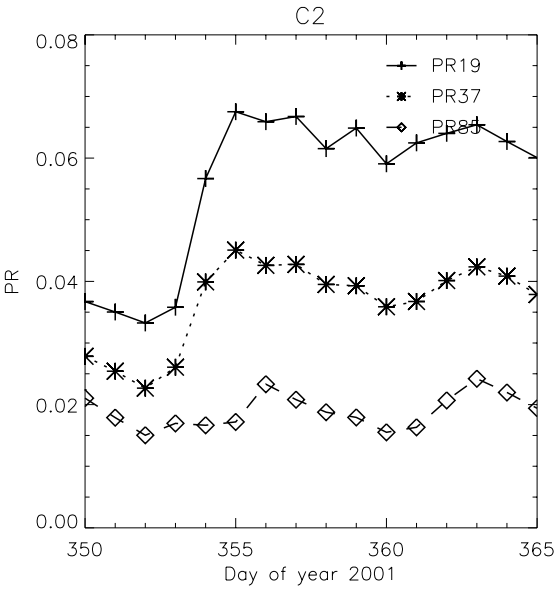

Figure 29. DMSP-SSM/I polarisation ratio in C2.

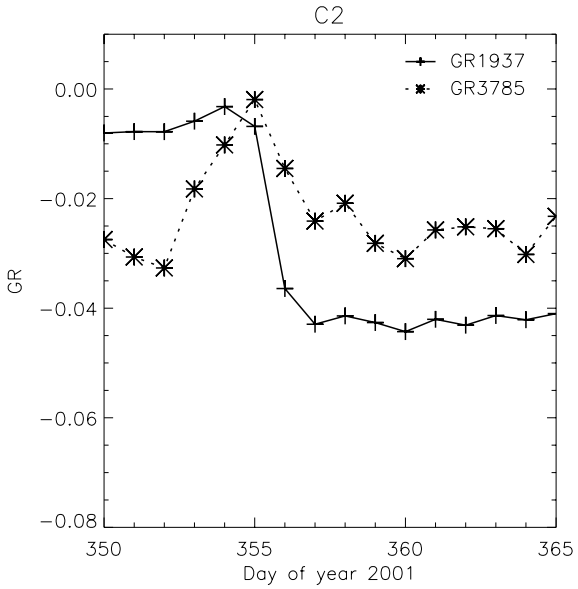

Figure 30. DMSP-SSM/I gradient ratio in C2.

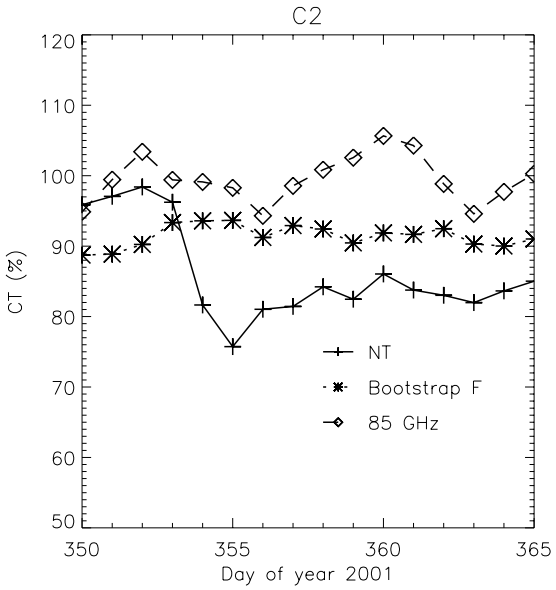

Figure 31. DMSP-SSM/I ice concentration in C2 using the NASA team, bootstrap and near 90GHz algorithms.

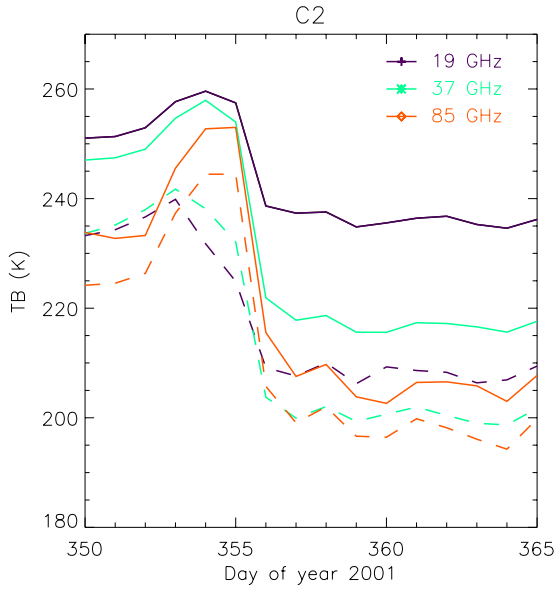

Figure 32. DMSP SSM/I brightness temperature in C2.

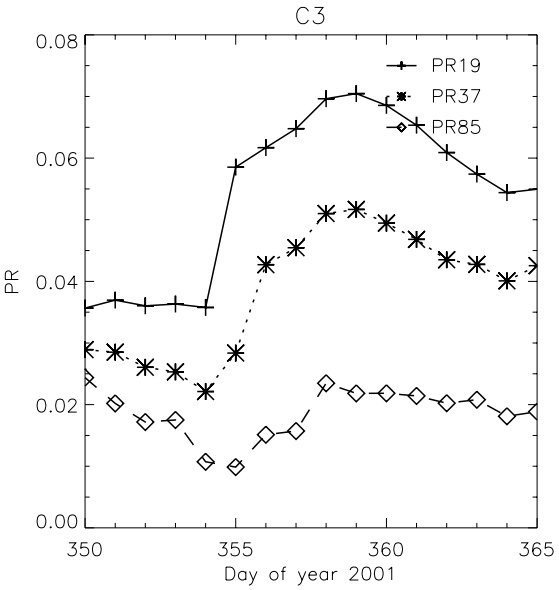

Figure 33. DMSP-SSM/I polarisation ratio in C3.

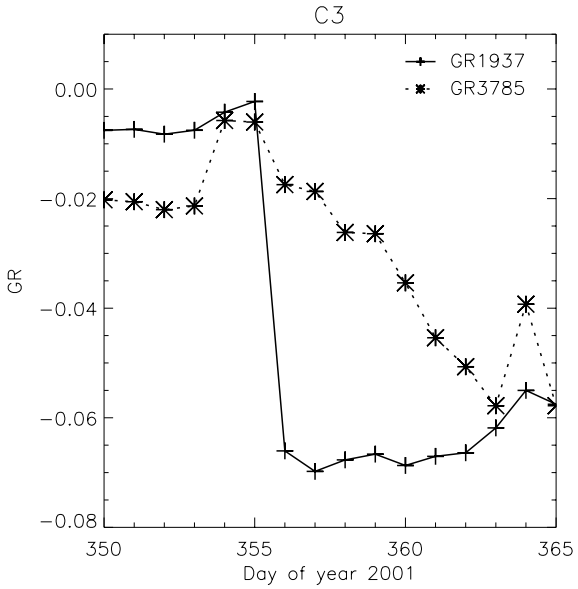

Figure 34. DMSP-SSM/I gradient ratio in C3.

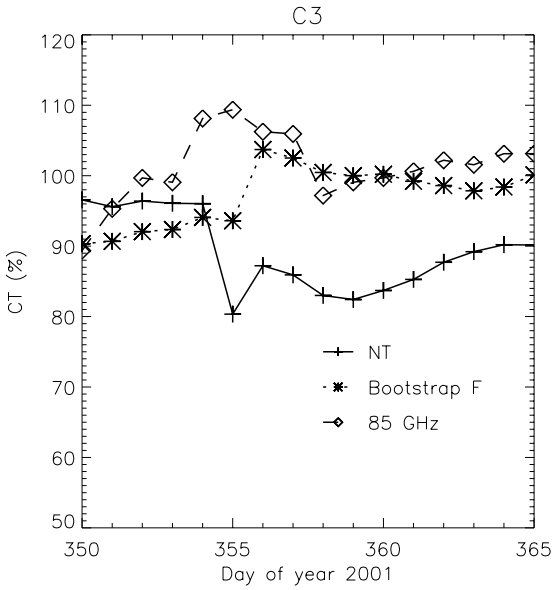

Figure 35. DMSP-SSM/I ice concentration in C3 using the NASA team, bootstrap and near 90GHz algorithms.

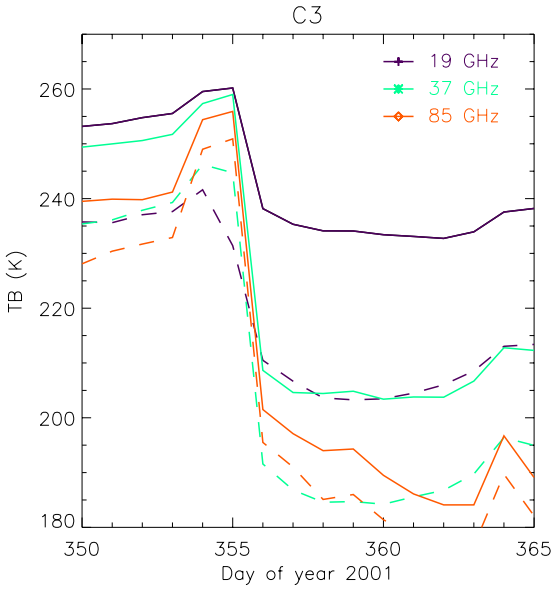

Figure 36. DMSP SSM/I brightness temperatures in C3.

5.4 Arctic Ocean and Barents Sea

December 6th 2002 the temperature in Fram Strait, North of Svalbard and Greenland and in the Barents Sea increase from between -40 and -10˚C to 1-2˚C and then decrease to between -20 and -10˚C 1-2 days later. The temperature records from the metrological stations on land in North Greenland, Svalbard and Novaja Semlja are shown in figure 37. The warm Atlantic air is driven by a stable high pressure over Scandinavia (~1045Hpa) and Low pressure systems both in Denmark Strait (992Hpa→958Hpa) and Disko Bay (959Hpa) and later (Dec. 7th) also in North Greenland (983Hpa). The North Greenland low pressure moves toward the North Pole in the days after December 7th. In the Arctic Ocean (D1 and D2) the backscatter shown in figures 38 and 39 drop from ~-9dB to ~-14dB during the melt and recover to the initial level after refreeze. In Barents Sea (D3) SeaWinds σ_0 shown in figure 40 increase from an initial level about -16dB to -10dB after refreezing. APR in D1 (figure 38) drop at the peak of melt from 0.15 to 0.1, but recover to the initial level after refreezing. APR in D2 (figure 39) is unaffected by the backscatter decrease. In area D3 APR increase from 0.21 to 0.27 after re-freezing shown in figure 40. The brightness temperature in D1 and D2 shown in figures 44 and 48 increase 25-60K during melt and gradually decrease after refreeze. The increase is greatest for 37GHz and in particular 85GHz. $GR_{19\text{-}37GHz}$ shown in figure 42 and 46 for area D1 and D2 increase to ~0 during melt and decrease below the initial level after refreeze. PR_{19GHz} in figures 41 and 45 increase during melt and gradually decrease after refreezing. At melt on-set in D1 bootstrap IC in figure 43 increase by 10% before it drops momentarily 15% below the initial level at refreeze. After refreeze it quickly recovers to the initial level. In D2 the bootstrap IC in figure 47 increase by 10% during melt but recover to the initial level after re-freeze. NASA team is depressed by 20% during and after the melt in both D1, D2 and D3 (figures 43, 47 and 51). In D1 the NASA team IC further drop momentarily by 20% at re-freeze. In D1 near 90GHz IC increase by 15% during melt and decrease by 30-50% at - and after refreeze. In D2 the near 90GHz IC increase 15% during melt but stabilize at the initial level after refreeze.

The German research vessel Polarstern went into the Barents Sea in March 2003 several months after the December melt event in D3. The observed snow cover on the first-year ice was characterised by extensive internal layering, depth hoar crystals (diameter>5mm) at the

snow/ice interface and liquid brine on the very rough ice surface. 5-10 cm of new snow covered the weathered snow and ice (C. Haas, personal communications 2003).

The meteorological and satellite parameters from D1, D2 and D3 are shown in figures 37-52.

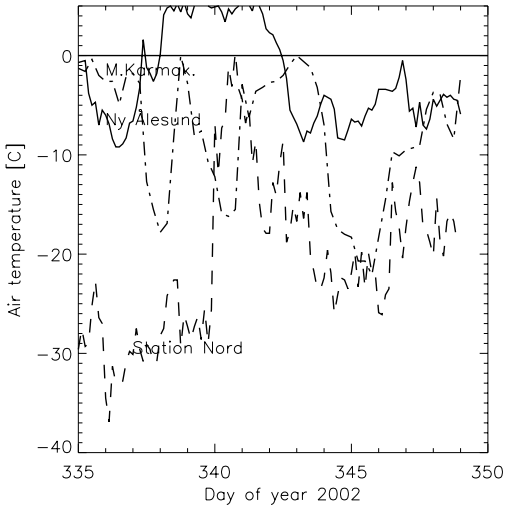

Figure 37. Air temperature [˚C] from meteorological land stations in Greenland Svalbard and Novaja Semlja. Records from Station Nord, Ny Ålesund and Malye Karmakuly.

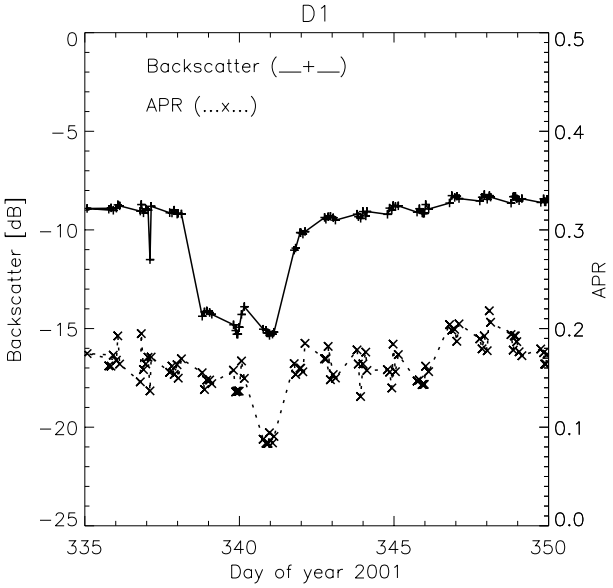

Figure 38. QuikScat SeaWinds HH- backscatter and APR in D1-Arctic Ocean 82N.

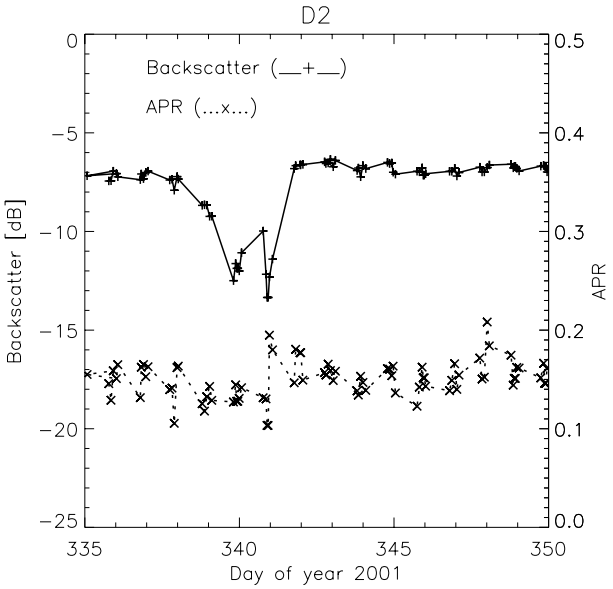

Figure 39. QuikScat SeaWinds HH- backscatter and APR in D2-Arctic Ocean 85N.

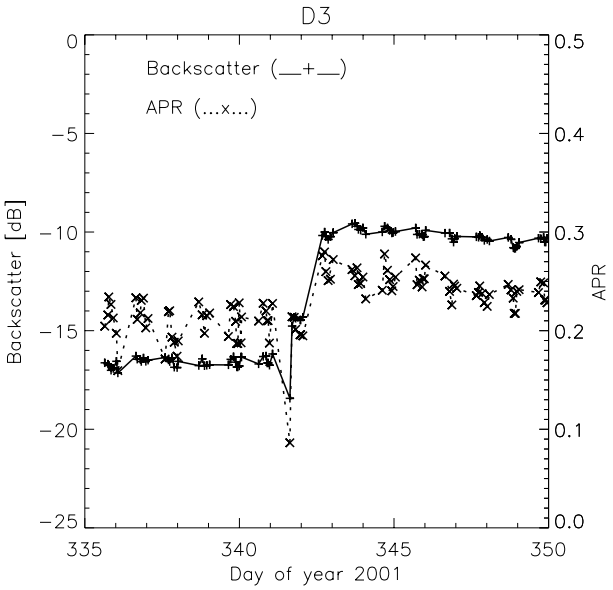

Figure 40. QuikScat SeaWinds HH- backscatter and APR in D3-Barents Sea

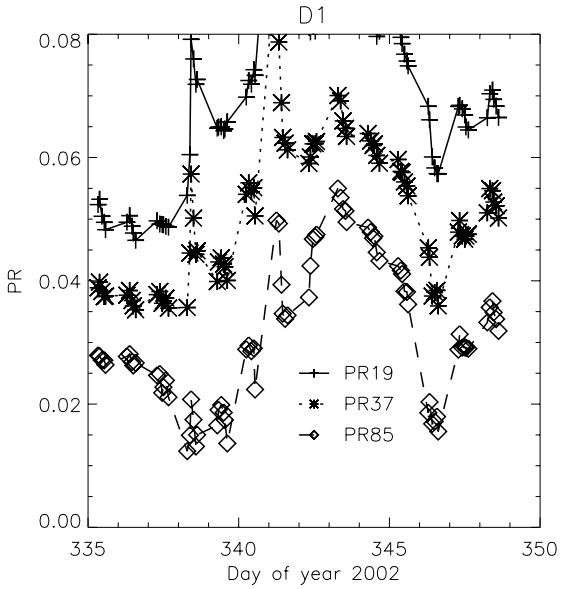

Figure 41. DMSP-SSM/I polarisation ratio in D1.

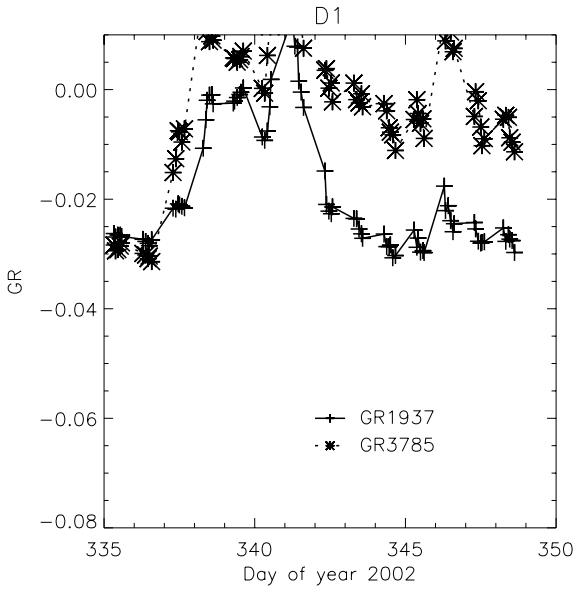

Figure 42. DMSP-SSM/I gradient ratio in D1.

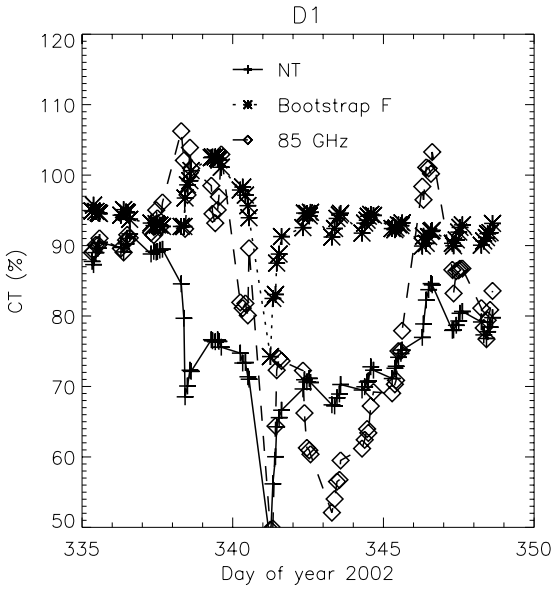

Figure 43. DMSP-SSM/I ice concentration in D1 using the NASA team, bootstrap and near 90GHz algorithms.

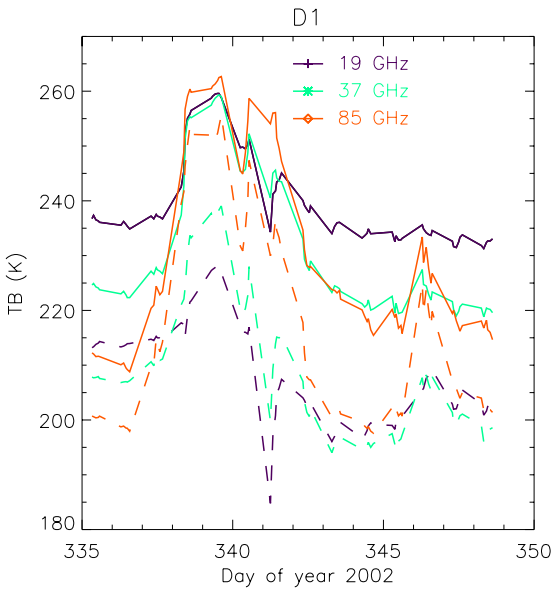

Figure 44. DMSP-SSM/I brightness temperatures in D1.

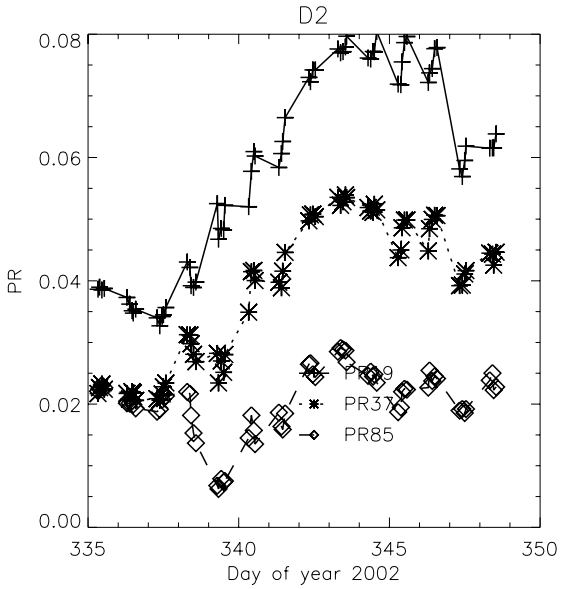

Figure 45. DMSP-SSM/I polarisation ratio in D2.

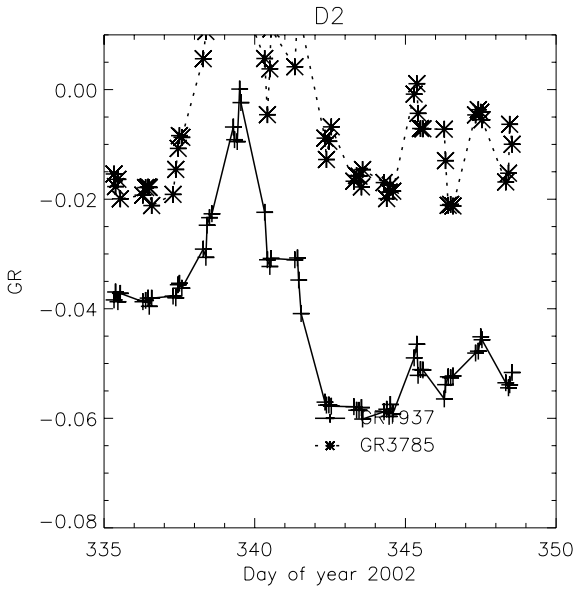

Figure 46. DMSP-SSM/I gradient ratio in D2.

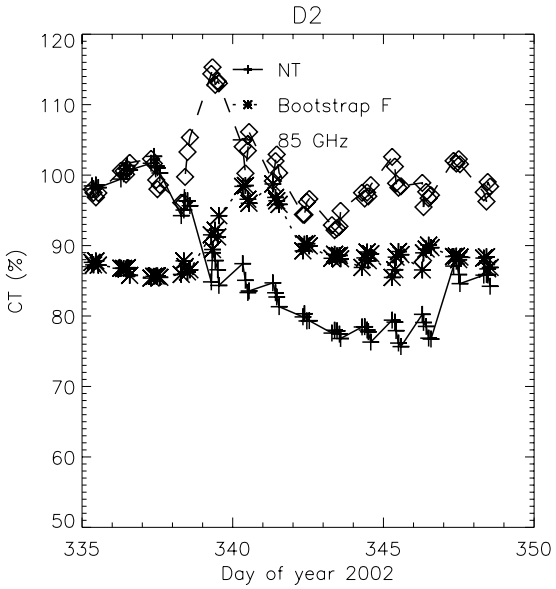

Figure 47. DMSP-SSM/I ice concentration in D2 using the NASA team, bootstrap and near 90GHz algorithms.

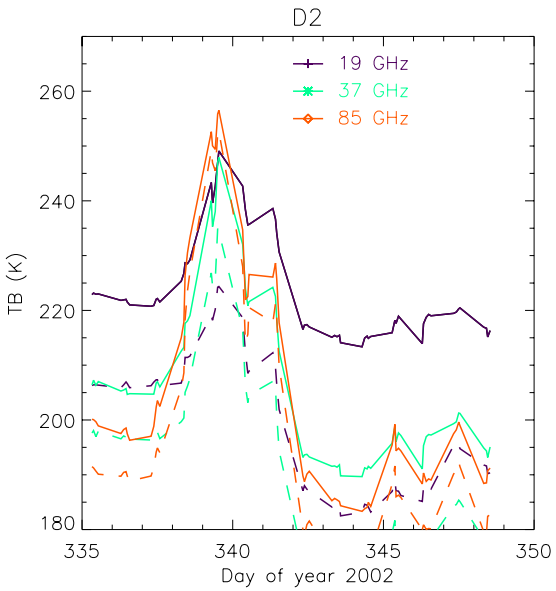

Figure 48. DMSP-SSM/I brightness temperatures in D2.

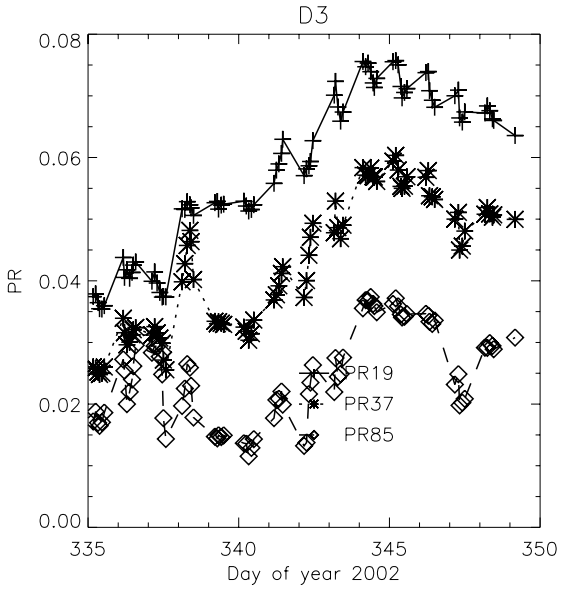

Figure 49. DMSP-SSM/I polarisation ratio in D3.

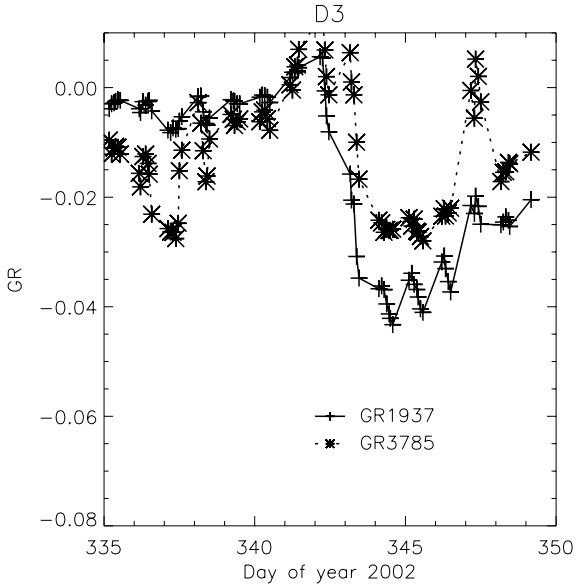

Figure 50. DMSP-SSM/I gradient ratio in D3.

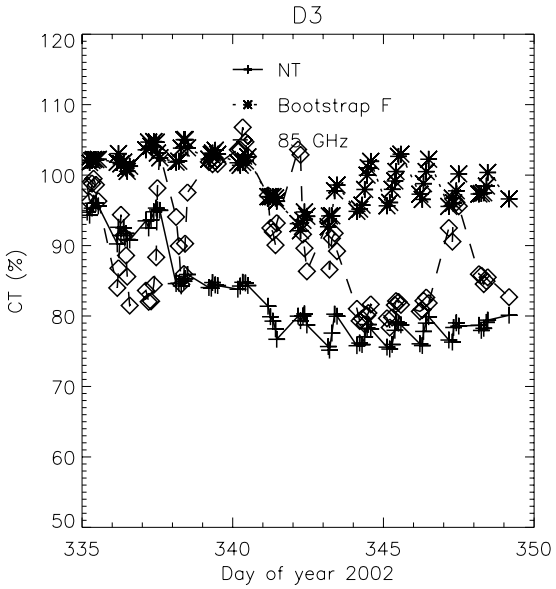

Figure 51. DMSP-SSM/I ice concentration in D3 using the NASA team, bootstrap and near 90GHz algorithms.

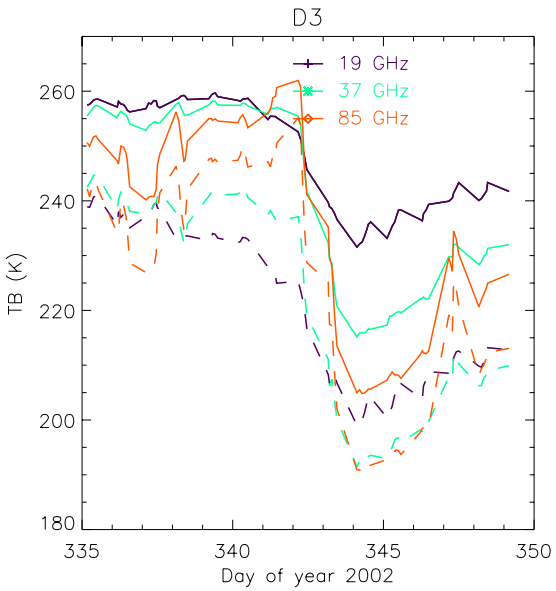

Figure 52. DMSP-SSM/I brightness temperatures in D3.

5.5 Comparison of four events

The evolution of first-year ice SeaWinds σ_0 and Tb during the four melt events is similar in the first-year ice areas B1, C1, C2, C3 and D3. SeaWinds σ_0 increase during melt to ~8 times higher level after refreezing (typically -18dB→ -9dB). The brightness temperature at 19, 37 and 85GHz increase during the melt by 5-10K, but decrease at refreeze 10-50K below the initial level. The changes are greater for Tb_{37GHz} and Tb_{85GHz} than for Tb_{19GHz}. $GR_{19\text{-}37GHz}$ decrease from a level typical for first-year (~0) ice to a level more typical for multi-year ice (-0.02, -0.07). $PR_{19\text{-}37GHz}$ increase at refreezing from 0.04 to 0.06.

Both the evolution of APR and the ice concentration estimates using the bootstrap, NASA team and near 90GHz algorithms differ in the areas dominated by first-year ice (B1, C1, C2, C3 and D3). APR evolves in 3 different ways: 1) in area B1 and C1 APR is unaffected by the

melt event, 2) in C2 and C3 APR drop during the melt but stabilize at a higher level after than before the event, and 3) in area D3 APR increase to a higher level than before the event. The bootstrap concentration algorithm is the most stable in the 5 first-year ice study areas during and after melt. In area B1, C1, C2, and D3 the bootstrap IC remains at approximately the same level before under and after the melt events (90-100%), in C3, however, the bootstrap IC jump from 93→105% at refreeze. The NASA team IC decrease in all first-year ice cases from ~100 to ~80% during and after the melt. In all first-year ice areas the near 90GHz IC increase during the melt event by 10%, but stabilize after refreeze at the same level as before the event.

The evolution of backscatter and brightness temperatures in the Arctic Ocean multi-year ice (D1 and D2) is similar. The melt in D1 is however more severe than in D2 which gives significant differences in the evolution of the ice concentration computed with the three ice concentration algorithms. The evolution of the near 90GHz IC in D1 and D2 is very different, while the evolution of bootstrap and NASA team IC follow the same pattern in the two areas (except the momentary drop in ice concentration before refreeze in D1). The NASA team IC is however depressed compared to bootstrap even after refreeze.

The ice drifting along the East Coast of Greenland is in general a mixture of both multi-year ice and first-year ice. The satellite parameter evolution in A1 and A2 in Denmark Strait and the Greenland Sea is to some extent a combination of the parameter evolution of first- and multi-year ice. For example, the backscatter decrease during melt like multi-year ice but after refreezing it rise to a higher level than before melt like first-year ice.

6. Discussion

Several parameters including $Tb_{19,37,85GHz}$, PR_{19GHz}, $GR_{19\text{-}37GHz}$, $GR_{37\text{-}85GHz}$ and σ_0 experience large changes during the temporary melt events i.e. temporal gradients (parameter/time) are important for melt detection. In particular σ_0 and its response to melting are significantly different for multi-year ice and first-year ice as summarized in section 5. However if we disregard the absolute σ_0 level and only consider the temporal gradient, $\Delta\sigma_0/\Delta t$, we see that it is large at refreeze and represents a strong indicator for melt detection. Also temporal gradients of $GR_{19\text{-}37GHz}$ $GR_{37\text{-}85GHz}$ are important indicators: $GR_{37\text{-}85GHz}$ increase at the melt onset and $GR_{19\text{-}37GHz}$ decrease at refreeze for both multi-year ice and first-year ice areas. The decrease in the $GR_{19\text{-}37GHz}$ temporal gradient at refreeze is used in the introduction to detect the frequency of melt events in areas covered >95% with ice (bootstrap). All parameters are in addition to being related to ice type also dependent on ice concentration. The behaviour of PR during melt, Tb at refreeze, GR during melt, and multi-year ice σ_0 during melt may mimic an intermediate or low concentration sea ice cover. The bootstrap algorithm on the other hand remains stable or increase during and after melt. The use of any of the parameters mentioned above for melt detection should be checked against the bootstrap ice concentration estimate. In water areas only partially covered by ice, melt detection will be difficult due to the ambiguous reaction of most parameters to both ice concentration and melt. The Radarsat scenes covering C1 before and after melt further indicate that the depression in NASA team IC is unrealistic. The Radarsat scenes covering C1 before and after the melt indicate a stable ice concentration > 95%.

6.1 Backscatter

The backscatter model is simple, it includes no treatment of multiple scattering, dense media scattering, it has a uniform distribution of scatterers and the surface model is not always within the valid range. Anyway, the model simulates adequately the absolute backscatter level of first-year and multi-year sea ice when compared to field measurements from literature (measurements from Onstott, 1992). The backscatter evolution is simulated for increasing snow grain size and ice roughness in both C-band and Ku-band. The differences between the frequencies are evident. In particular increased snow grain size and to a minor extent the ice surface roughness increase Ku-band backscatter shown in figure 53. Increased ice surface roughness increase C-band backscatter shown in figure 54.

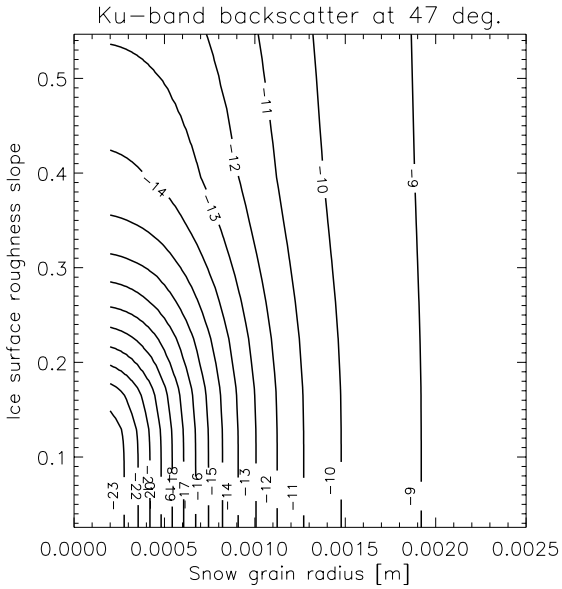

Figure 53. Modelled QuikScat SeaWinds Ku-band backscatter at 47˚ sensitivity to snow grain size and ice surface roughness slope (1.5-power correlation function). The surface roughness used in the model is the measured values given in figure 3. Other ice parameters are given in chapter 3 and snow grain sizes increase monotonically.

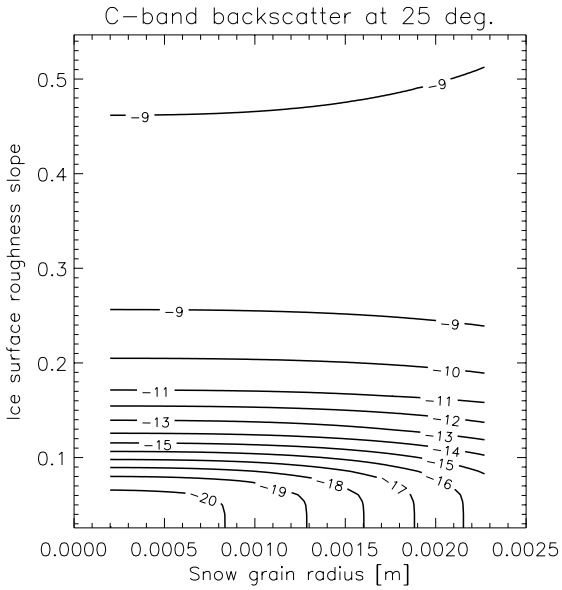

Figure 54. Modelled Radarsat ScanSAR backscatter at 25˚ sensitivity to snow grain size and ice surface roughness slope (1.5-power correlation function). The surface roughness used in the model is the measured values given in figure 3. Other ice parameters are given in chapter 3 and snow grain sizes increase monotonically.

The model interpolation of first-year ice Radarsat ScanSAR backscatter measurements before and after the C1 warm air event in figure 55 indicate that the ice surface roughness has increased. The first-year ice backscatter increase measured after refreezing in areas B1, C1-3 and D3 and the model results in figure 53 indicate that the snow grains are enlarged. Increased ice surface roughness does increase Ku-band σ_0, but an additional snow grain size increase is needed in order to increase the modelled Ku-band σ_0 to the measured backscatter level and further reduce Tb as observed. The modelling of σ_0 in both C and Ku-band indicate that the changes are caused by a combination of snow grain size enlargement and increased ice surface roughness. These changes in the ice properties are permanent.

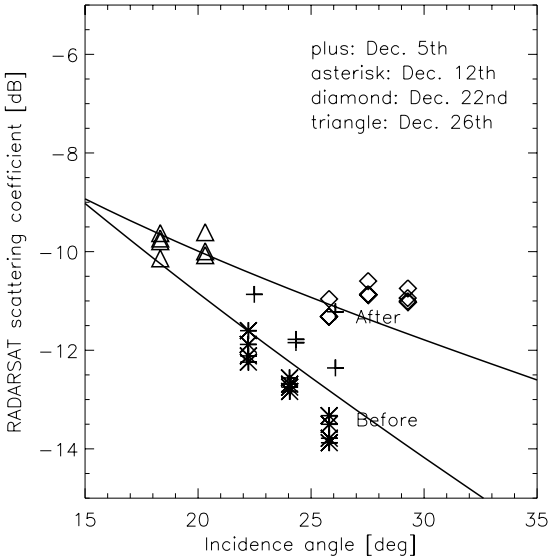

Figure 55. Modelled and observed Radarsat ScanSAR backscatter. The ice surface roughness parameters have been selected to fit the observations. The SAR pixels have merged into 25km pixels.

The backscatter model indicate that the reported structural modification of first-year ice after temporal melt leading to lower permittivity (Arcone et al., 1986; Light et al., 2003) has a small but positive effect on the Ku-band σ_0 due to more ice volume scattering. This process is however minor compared to the increased ice surface roughness caused by the expulsion of a surface brine layer combined with brine wicking. This process reduces volume scatter slightly but increase in return ice surface scattering significantly.

The SeaWinds backscatter from multi-year ice is dominated by volume scattering. The modelled penetration depth and volume scattering is significantly reduced when the snow layer is moist or wet. The multi-year ice σ_0 decrease during melting is most likely caused by a wet snow layer.

6.2 Tb

Fuhrhop et al. (1997) found that the following snow and ice properties were significant for Tb: 1) liquid water in/on snow and ice, 2) snow grain size and density, 3) In case the snow is sufficiently thin, air bubbles in ice, and 4) ice salinity. The properties are ordered according their significance for Tb when varied within measured ranges.

Figure 56 is showing the modelled sensitivity using MWMOD of Tb_{19V} to first-year ice snow grain size and volumetric liquid water content in the snow. The snow and ice temperatures are kept at the melting point. Tb_{19V} is primarily sensitive to transition of the snow cover from dry to moist. Tb_{19V} increase by 20K by introduction of 1% liquid water in the snow from the dry snow around 230K to moist around 250K. The two-layer model finds that Tb_{19V} increase by 15K from a dry to a moist (1% liquid water) snow cover. At the onset of melt the observed Tb_{19V} increase by 5-20K. The model results in figure 56 show that first-year ice Tb increase by introducing liquid water in the snow layer and moist snow is only to a minor extent sensitive to changes in the snow grain size and increasing liquid water content. The modelled increase in Tb_{19V} is in good agreement with the observed increase in Tb_{19V} at the onset of melt.

Figure 57 is showing the modelled sensitivity of first-year ice Tb_{19V} to snow grain size versus thermometric snow temperature below freezing (0˚C) using MWMOD. The thermometric temperature in the ice follows the snow temperature at a slower rate. Tb_{19V} is primarily sensitive to the increasing snow grain size. The liquid brine volume and dielectric loss reduction in the ice, which is a consequence of decreasing temperature, are minor effects. The modelled first-year ice Tb_{19V} (MWMOD) is decreasing from small to intermediate grain sizes and increase again for larger grain sizes. The maximum Tb_{19V} decrease is about 20K at intermediate grain sizes. The observed first-year ice Tb_{19V} is decreasing from before to after the melt by 10-20K. The modelled increase in Tb_{19V} for large snow grain sizes is surprising. The result is in contrast to the trend from the 2-layer model and earlier studies described in the literature (e.g. Mätzler, 1987). Both the 2-layer model and Mätzler (1987) indicate that Tb decrease monotonically for increasing snow grain sizes. The two-layer model is exaggerating scattering in the snow layer so that reduction in Tb for increasing snow grain sizes is unrealistic using a 13cm snow layer. Recalling the rule of thumb by Mätzler (1987) that the reduction, $\Delta Tb_{18GHz} \approx 10d$, where d is the depth of the coarse grain layer in [cm], we now reduce the effective snow layer depth to 2cm in the 2-layer model and re-compute Tb_{19V} as a function of thermometric air temperature and snow grain size. The results are shown in figure 58 and fits well with the observed reduction. The speculation behind the reduced snow layer thickness is that layering is inherent in snow packs (Wiesmann & Mätzler, 1999) and the 2cm should be regarded as an effective thickness of coarse-grained snow. The sharp reduction in first-year ice Tb (19GHz, 37GHz and 85GHz) at refreeze compared to before and during melt is interpreted as the instant where the liquid water in the snow freeze, attenuation decrease and scattering in the snow layer is increased due to the fully exposed and enlarged metamorphosed snow grains. The observed reduction in Tb can be explained by a grain size increase as modelled with the 2-layer model.

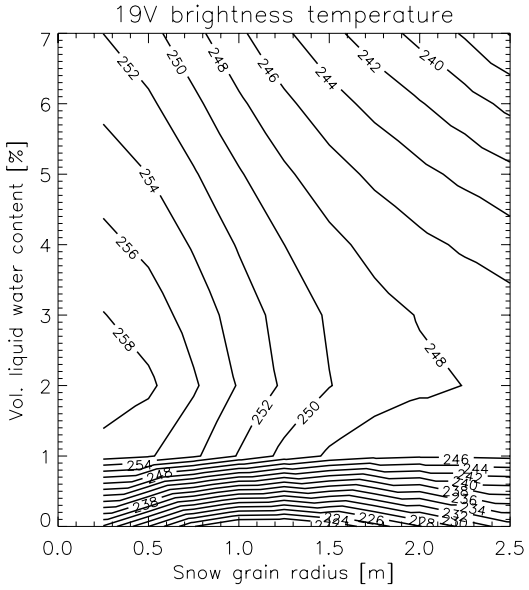

Figure 56. Modelled (MWMOD) SSM/I Tb_{19V} sensitivity to snow grain size and volumetric liquid water content in the snow on first-year ice. Ice and snow parameters are given in chapter 3.

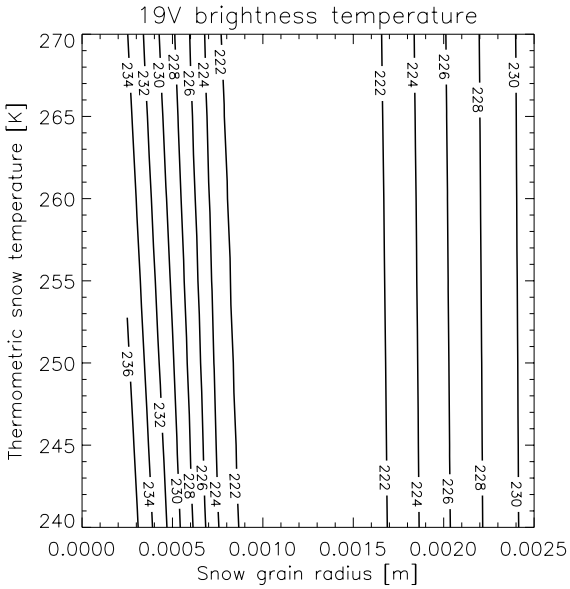

Figure 57. Modelled (MWMOD) SSM/I Tb_{19V} sensitivity to snow grain size and thermometric snow temperature on first-year ice. Ice and snow parameters are given in chapter 3.

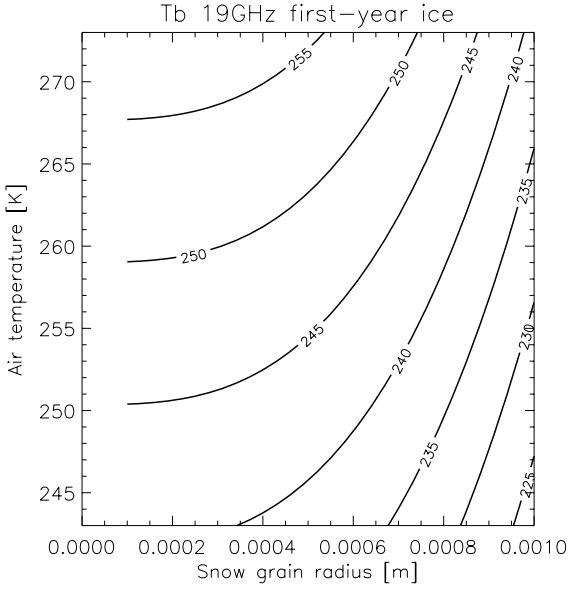

Figure 58. Modelled (2-layer model) SSM/I Tb_{19V} sensitivity to snow grain size and thermometric air temperature on first-year ice. Ice and snow parameters are given in chapter 3, however the effective snow depth is set to 2cm. Note that the modelled snow grain size is <1mm due to restrictions of the Rayleigh scattering model.

6.3 Satellite observations

The change in the ice parameters responsible for the increased first-year σ_0 is gradual and evolves during the warm period. The gradual change is most clearly shown in C1, C2 and C3 with σ_0 increasing during 2-3 successive warm days. The evolution of e.g. APR and GR are also gradual but experience both negative and positive trends during the actual melt. While first-year σ_0 increase monotonically during melting to multi-year ice levels APR seems to be more sensitive to the actual dominant scattering mechanism. First-year ice APR is normally ~0.23 and multi-year ice is ~0.17. During melt first-year APR is reduced but recovers to the

same or a higher level after refreeze. Multi-year ice APR is reduced during melting but recover to the initial level after refreezing. After weathering first-year ice σ_0 is dominated by both rough surface scattering and snow volume scattering while multi-year ice is dominated by ice and possibly snow volume scattering. These differences are reflected in APR. When the snow is wet and the scattering processes are confined to the upper portion of the snow or ice in both multi- and first-year ice, APR values are comparable. After refreeze where first-year ice Ku-band σ_0 is at the same level as multi-year ice, we notice that first-year ice APR is still higher than multi-year ice APR. The scattering mechanisms reflected in APR for the two ice types producing the same backscatter level are apparently different. This is in contrast to the level of $GR_{19\text{-}37GHz}$ for first- and multi-year ice after weathering. $GR_{19\text{-}37GHz}$ is also sensitive to differences in radiative processes and is e.g. in the NASA team algorithm used to separate multi-year ice and first-year ice. However, after weathering there is no significant $GR_{19\text{-}37GHz}$ difference between first-year and multi-year ice.

The increase in Tb in all four regions during melt is a combination of cloud liquid water, thermometric surface temperature increase (Liu & Curry, 2003) and reduced penetration depth due to the appearance of liquid water in the snow. The warmer surface temperature and the atmospheric cloud liquid water can raise Tb_{19GHz} by about 8K. On the other hand, the MWMOD simulations in figure 56 indicate that Tb_{19V} can increase by 20K when dry snow is moistened by melt. If the observed changes in the radiometer parameters GR and PR and NASA team IC during melt were only due to increased atmospheric water vapour and cloud liquid water we would expect to se PR_{19GHz} decrease, $GR_{19\text{-}37GHz}$ increase especially for multi-year ice and IC increase (Oelke, 1997). $GR_{19\text{-}37GHz}$ does indeed increase for multi-year ice during melt, but also PR_{19GHz} increase and IC decrease contrary to predictions for the atmospheric influence on these parameters. The atmospheric influence seems to be secondary to the 19GHz emissivity changes in the ice during melt.

The melt is more severe in D1 than D2. We speculate that the momentary drop in IC (all 3 algorithms) in D1 by ~20-40% and Tb by 10K, anti-correlated to the peaks in $PR_{19,37,85GHz}$ from 0.02 to 0.04 indicate liquid water on the melting surface.

The Tb polarisation difference increase in the presence of smooth horizontal layers within the snow. The effect of layering on the polarisation difference is larger for lower frequency (<37GHz) because of the lower absorption and scattering. The polarisation difference is smaller for higher frequency (>37GHz). High frequencies suffer from shallow penetration and isotropic scattering and absorption in the snow layer (Mätzler, 1987). PR_{19GHz} experience a gradual increase in all areas A, B, C and D while PR_{85GHz} is nearly stable before and after the melt. Horizontal ice layers in the snow pack are a common consequence of snow melt and extensive layering was observed in Barents Sea near D3 after the event (C. Haas, personal communications 2003). The layers are a plausible cause of the PR_{19GHz} increase. In any case it is worth noticing that PR_{85GHz} is less sensitive to melt events than PR_{19GHz}. This is important because PR_{19GHz} is used as input to the NASA team IC algorithm and the difference $Tb_{85V} - Tb_{85H}$ is used in the near 90GHz algorithm.

6.4 Ice concentration algorithms

The absolute level of concentrations computed by the three algorithms (bootstrap, NASA team and near 90GHz) is dependent on the selection of tie-points. The relative variations observed during and after the melt events are related to the sensitivity of these algorithms to specific changes in the ice radiative and scattering properties, e.g. snow grain size brine layer expulsion leading to roughness increase and ice layers in the snow as discussed above. Boot-

strap is least sensitive to the melt with 10% IC increase during the warm period, and it recovers to the initial concentration level after refreezing. NASA team is more sensitive with a 20% IC decrease during melt. In addition, the NASA team IC depression persist after refreezing for both first- and multi-year ice compared to bootstrap and near 90GHz IC. The near 90GHz algorithm is quite sensitive to atmospheric constituents like cloud liquid water and water vapour and the near 90GHz IC is in general more variable than IC from the two other algorithms. Both increased cloud liquid water and water vapour in the atmosphere increase near 90GHz IC and this is at least partly the explanation for the increased IC during the cyclone passage causing the ice surface melt. After refreeze near 90GHz IC stabilize at the initial level in areas A2, B1, C1, C2, C3 and D2. In D1 and D3 near 90GHz IC is highly variable throughout the studied period, apparently with little correlation to the melt and freeze processes. It can not be ruled out that the variations in the near 90GHz IC are indeed real variations in the ice concentration. D1 is a special case because we believe that there is liquid water on the ice surface and the snow layer is absent. D3 may have experienced a sequence of melt freeze cycles during the period even though this is not clearly reflected in σ_0 or Tb. It seems that near 90GHz IC is more vulnerable to atmospheric constituents than to the modified ice surface emissivity. Except during the cyclone passage, the boot-strap and near 90GHz are close in performance.

7. Conclusions

Radiative and scattering processes on first-year ice and multi-year ice are not identical during melt events. Anyway, temporal gradients of central satellite parameters in particular σ_0, Tb and GR, are useful for melt detection. To overcome ambiguities between melt events and actual reduction in ice concentration temporal gradients of σ_0, Tb and GR should be checked against ice concentration estimates from the bootstrap algorithm, which is the least sensitive algorithm to changes in the physical properties of the weathered ice. The ice concentration estimate of the near 90GHz algorithm is in most cases insensitive to weathered ice after refreeze. However, there were significant variations in near 90GHz IC in D1 and D3 after refreeze, possibly caused by atmospheric constituents.

The positive temporal gradient of $GR_{19\text{-}85GHz}$ (daily increase > 0.02) detects the onset of melt on both first-year and multi-year ice. The negative slope of the temporal gradient $GR_{19\text{-}37GHz}$ (daily decrease > 0.02) detects the freeze-up for bootstrap ice concentrations >95%.

Models simulations indicate that the significant reason for the Ku-band σ_0 increase over first-year ice is a combination of increased ice surface roughness and snow grain size. The wet snow layer causes the multi-year Ku-band σ0 decrease during melt. The C-band σ_0 at 25˚ is affected by ice surface roughness. The wet snow layer and the resulting reduction in snow volume scattering cause the Tb19GHz, Tb37GHz and Tb85GHz increase during melt. The Tb_{19GHz}, Tb_{37GHz} and Tb_{85GHz} decrease at refreezing is on the other hand caused by increased volume scattering by the snow grains with increased diameter. Internal ice layers are responsible for the PR increase at 19 and 37GHz.

The Tb sensitivity to central snow parameters, i.e. moisture and snow grain size computed by the MWMOD and 2-layer models is clear. However, MWMOD is predicting unrealistic oscillations in Tb for increasing grain sizes and the 2-layer model is apparently overestimating scattering. The general performance of these Tb models is not satisfactory and it is an important future task find a suitable method to model Tb.

7.1 Project prospective

Oelke (1997) found that IC computed using the NASA team algorithm erroneously could increase by 10% due to the influence of atmospheric constituents on the measured Tb. We find that the NASA team algorithm is depressed by 20% due to irreversible changes in the snow and ice properties and the ice emissivity during temporary ice surface melt in winter. The consequences of the emissivity changes are serious not only for the computed ice concentration but for any interpretation of sea-ice microwave signatures. The persistence of the weathered foot-print after the actual melt makes systematic interpretation of microwave signatures difficult especially along the ice edge where temporary melt is common. Identification of the actual melt events is feasible using e.g. the daily gradient of $GR_{19\text{-}37GHz}$, but distinction between weathered first-year ice and multi-year ice is difficult after refreeze. Because correction of the emissivity before computation of IC and identification of weathered ice after refreeze is difficult it is therefore important to select an IC algorithm which is fairly insensitive to changes in the ice emissivity.

Two of the three ice concentration algorithms used in this investigation show potential for further investigation due to their low sensitivity to emissivity changes of the ice. This is the bootstrap algorithm and the near 90GHz algorithm. The near 90GHz is sensitive to atmos-

pheric constituents like water vapour and cloud liquid water but near 90GHz IC has on the other hand ~4times better resolution than both bootstrap and NASA team IC. Atmospheric contamination of the computed IC can be minimized through correction schemes using numerical model or satellite derived parameters describing the atmospheric constituents (Kern, 2001).

With the launch of the AMSR-E radiometer onboard the NASA Aqua satellite May, 2002 and AMSR onboard ADEOS II December 2002 brightness temperature at both 6, 10, 18, 23, 36 and 89GHz are acquired and distributed in near-real-time. 6GHz brightness temperature has low sensitivity to snow grain size enlargements within a natural range and ice concentration algorithms using 6GHz emissivity will be influenced less by such changes in the snow properties than e.g. the 19GHz emissivity. The advent of these radiometer measurements are of significant interest to the IOMASA project in light of the problems analysed in this report.

Acknowledgements

This work was supported financially by the Danish Research Foundation (Sagsnr. 5005-00-0009) and the European Commission IOMASA project (Contract No. EVK3-CT-2002-00067). The QuikScat SeaWinds data is the L2B product from NOAA-NESDIS. The DMSP-SSM/I data is from National Snow and Ice Data Center.

8. References

Anderson, M. R. & S. D. Drobot (2001). Spatial and temporal variability in snowmelt onset over Arctic Sea Ice. Annals of Glaciology 33, pp. 74-78.

Arcone, S. A., A. J. Gow & S. McGrew (1986). Structure and Dielectric Properties at 4.8 and 9.5 GHz of Saline Ice. *Journal of Geophysical Research 91*(C12), pp. 14 281-14 303.

Armstrong, R. L., A. Chang, A. Rango, E. Josberger (1993). Snow Depth and Grain-Size Relationships with Relevance for Passive Microwave Studies. *Annals of Glaciology 17*, 171-176.

Barber, D. G., S. P. Reddan & E. F. LeDrew (1995). Statistical Characterisation of the Geophysical and Electrical Properties of Snow on Landfast First-Year Sea Ice. *Journal of Geophysical Research, 100*(C2), 2673-2686.

Cappelen, J., B. V. Jørgensen, E. V. Laursen, L. S. Stannius, & R. S. Thomsen (2001). The observed climate of Greenland, 1958-99 – with climatological standard normals, 1961-90. *Danish Meteorological Institute Technical Report 00-18*, p. 136. Copenhagen.

Carlström, A. & L. M. H. Ulander (1993). C-band Backscatter Signatures of Old Sea Ice in the Central Arctic During Freeze-Up. *IEEE Transactions on Geoscience and Remote Sensing 31*(4), 819-829.

Carsey, F. D. (1985). Summer Arctic Sea Ice Character from Satellite Microwave Data. *Journal of Geophysical Research, 90*(C3), 5015-5034.

Cavalieri, D.J & P. Gloersen (1984). Determination of Sea Ice Parameters with the NIMBUS 7 SMMR. *Journal of Geophysical Research 89*(D4), pp. 5355-5369, 1984.

Chuah, H.-T., S. Tjuatja, A. K. Fung, & J. W. Bredow (1996), A Phase Matrix for a Dense Discrete Random Medium: Evaluation of Volume Scattering Coefficient. *IEEE Transactions on Geoscience and Remote Sensing, 34*(5), 1137-1143.

Colbeck, S. C. (1982). An Overview of Seasonal Snow Metamorphism. *Reviews of Geophysics and Space Physics, 20*(1) 45-61.

Colbeck, S. C. (1989). Snow-Crystal Growth with Varying Surface Temperatures and Radiation Penetration. *Journal of Glaciology 35*(119), pp. 23-29.

Colbeck, S. C. (1990). The Layered Character of Snow Covers. *Reviews of Geophysics 29*(1), 81-96.

Comiso, J.C. (1986). Characteristics of Arctic Winter Sea Ice from Satellite Multispectral Microwave Observations. *Journal of Geophysical Research 91*(C1), pp. 975-994.

Comiso, J.C., D. J. Cavalieri, C. L. Parkinson, & P. Gloersen (1997). Passive Microwave Algorithms for Sea Ice Concentration: A Comparison of Two Techniques. *Remote Sensing of Environment 60*, pp. 357-384.

Dierking, W. M. I. Petterson & J. Askne (1999). Multifrequency Scatterometer Measurements of Baltic Sea Ice During EMAC-95. *International Journal of Remote Sensing, 20*(2), 349-372.

Dierking, W., A. Carlström & L. M. H. Ulander (1997). The Effect of Inhomogeneous Roughness on Radar Backscattering from Slightly Deformed Sea Ice. *IEEE Transactions on Geoscience and Remote Sensing 35*(1), 147-159.

Drinkwater, M. D. (1989), LIMEX '87 Ice Surface Characteristics: Implications for C-band SAR Backscatter Signatures. *IEEE Transactions on Geoscience and Remote Sensing 27*(5), 501-513.

Drinkwater, M. R., R. Hosseinmostafa & P. Gogeneni (1995). C-band Backscatter Measurements of Winter Sea-Ice in Weddell Sea, Antarctica. *International Journal of Remote Sensing 15*(17), 3365-3389.

Forster, R. R., D. G. Long, K. C. Jezek, S. D. Drobot, & M. R. Anderson (2001). The Onset of Arctic Sea-Ice Snowmelt as Detected with Passive- and Active-Microwave Remote Sensing. Annals of Glaciology 33, pp. 85-93.

Fuhrhop, R. T. Grenfell, G. Heygster, K-P. Johnsen, P. Schlüssel, M. Schrader & C. Simmer (1998). A Combined Radiative Transfer Model for Sea Ice, Open Ocean and Atmosphere. *Radio Science 33*(2), pp. 303-316.

Fung, A. K. & H. J. Eom (1982). Application of a Combined Rough Surface and Volume Scattering Theory to Sea Ice and Snow Backscatter. *IEEE Transactions on Geoscience and Remote Sensing 20*(4), 528-536.

Fung, A. K. (1994). *Microwave Scattering and Emission Models and Their Applications*. Norwood MA: Artec House.

Garrity, C. (1992). Characterisation of Snow on Floating Ice and Case Studies of Brightness Temperature Changes During the Onset of Melt. In: F. D. Carsey (Ed.). *Microwave remote sensing of sea ice, Geophysical monograph 68* (pp. 313-328). Washington DC: American Geophysical Union.

Grenfell, T. C. & A. W. Lohanick (1985). Temporal Variations of the Microwave Signatures of Sea Ice During Late Spring and Early Summer Near Mould Bay NWT, *Journal of Geophysical Research 90*(C3), 5063-5074.

Hallikainen, M. T. & P. A. Jolma (1986). Retrival of theWater Equivalent of Snow Cover in Finland by Satellite Microwave Radiometry. *IEEE Transactions on Geoscience and Remote Sensing 24*(6), pp. 855-862.

Hallikainen, M., & D. P. Winnebrenner (1992). The physical basis for sea ice remote sensing. In: F. D. Carsey (Ed.). *Microwave remote sensing of sea ice, Geophysical monograph 68* (pp. 29-44). Washington DC: American Geophysical Union.

Hallikainen, M., F. T. Ulaby & M. Abdelrazik (1986). Dielectric Properties of Snow in the 3 to 37 GHz Range. *IEEE transactions on Antennas and Propagation 34*(11), 1329-1340.

Hoekstra, P. & P. Cappillino (1971). Dielectric Properties of Sea and Sodium Cloride Ice at UFH and Microwave Frequencies. *Journal of Geophysical Research 76*(20), pp. 4922-4931.

Hollinger, J. P., J. L. Peirce & G. A. Poe (1990). SSM/I Instrument Evaluation. *IEEE Transactions Geoscience and Remote Sensing 28*(5), 781-790.

Holt, B. & S. A. Digby (1985). Processes and Imagery of First-Year Fast Sea Ice During the Melt Season. *Journal of Geophysical Research 90*(C3), 5045-5062.

Hurrell, J. W. (1995). Decadal trends in the North Atlantic oscillation: regional temperatures and precipitation. *Science 269*, 676-679.

Johnsen, K.-P. & G. Heygster (2000). Interference Effects in Freshwater and Sea Ice. In: C. Mätzler, COST Action 712, Radiative Transfer Models for Microwave Radiometry, Final Report (pp. 149-162). European Comission, EUR 19543 EN.

Josberger, E. G. & N. M. Mognard (2002). A passive Microwave Snow Depth Algorithm with a Proxy for Snow Metamorphism. *Hydrological Processes 16*, pp. 1557-1568.

Kern, S. (2001). A New Algorithm to Retrieve the Sea Ice Concentration Using Weather-Corrected 85GHz SSM/I Measurements. Ph.D. thesis, Institut für Umweltsphysik, Bremen, Germany.

Kim, Y. S., R. K. Moore, R. G. Onstott & S. Gogineni (1985). Towards Identification of Optimum Radar Parameters for Sea-Ice Monitoring. *Journal of Glaciology 31*(109), 214-219.

Koch, L. (1945). The East Greenland Ice, *Meddelelser om Grønland 130*(3).

Kunga, Y., F. T. Ulaby, T. F. Haddock, & R. D. DeRoo (1991). Millimeter-wave radar scattering from snow 1. Radiative transfer model. *Radio Science 26*(2), 329-341.

Künzi, K. F., S. Patil, & H. Rott (1982). Snow cover parameters retrieved from Nimbus-7 Scanning Multichannel Microwave Radiometer (SMMR) Data. *IEEE Transactions on Geoscience and Remote Sensing GE-20*(4), 452-467.

Leidner, S. M., R. N. Hoffman & J. Augenbaum (2000). SeaWinds Scatterometer Real-Time BUFR Geophysical Data Product. Users Guide, Version 2.3.0., NOAA/NESDIS.

Light, B., G. A. Maykyt and T. C. Grenfell (2003). Effects of Temperature on the Microstructure of First-Year Arctic Sea Ice. *Journal of Geophysical Research 108*(C2) 3051, doi: 10.1029/2001JC000887.

Livingstone, C. E. & M. D. Drinkwater (1991). Springtime C-band SAR Backscatter Signatures of Labrador Sea Marginal Ice: Measurements Versus Modelling Predictions. *IEEE Transactions on Geoscience and Remote Sensing 29*(1), 29-41.

Livingstone, C. E., K. P. Singh & A. L. Gray (1987). Seasonal and Regional Variations of Active/Passive Microwave Signatures of Sea Ice. *IEEE Transactions on Geoscience and Remote Sensing 25*(2), pp. 159-173.

Lohanick, A. W. & T. C. Grenfell (1986). Variations in Brightness Temperature Over Cold First-Year Sea Ice Near Tuktoyaktuk, NWT. *Journal Geophysical Research 91*(C4), 5133-5144.

Liu, G. & J. A. Curry (2003). Observation and Interpretation of Microwave Cloud Signatures over the Arctic Ocean durng Winter. Journal of Applied Meteorology 42, pp. 51-64.

Magagi, R. & M. Bernier (2003). Optimal Conditions for Wet Snow Detection Using RADARSAT SAR Data. *Remote Sensing of Environment 84*, 221-233.

Maslowski, W., D. C. Marble, W. Walczowski, & A. J. Semtner (2001). On large scale shifts in the Arctic Ocean and sea-ice conditions during 1979-98. *Annals of Glaciology 33*, 545-550.

Mätzler, C. (1987). Applications of the Interaction of Microwaves with the natural Snow Cover. *Remote Sensing Reviews 2*(2), pp. 259-391.

Mätzler, C., E. Schanda & W. Good (1982). Towards the Definition of Optimum Sensor Specifications for Microwave Remote Sensing of Snow. *IEEE Transactions on Geoscience and Remote Sensing 20*(1), pp. 57-66.

Maykyt, G. A. (1986). The Surface Heat and Mass Balance. In: N. Untersteiner (Ed.) *The Geophysics of Sea Ice*. NATO ASI series, series B: Physics Vol. 146. New York and London: Plenum Press.

Nghiem, S. V., R. Kwok, S. H. Yueh & M. R. Drinkwater (1995). Polarimetric Signatures of Sea Ice, 2 Experimental Observations, *Journal of Geophysical Research 100*(C7), 13681-13698.

Oelke, C. (1997). Atmospheric signatures in sea-ice concentration estimates from passive microwaves: modelled and observed. *International Journal of Remote Sensing 18*(5), pp. 1113-1136.

Onstott, R. G. & S. P. Gogeneni (1985). Active Microwave Measurements of Arctic Sea Ice under Summer Conditions. *Journal of Geophysical Research 90*(C3), 5035-5044.

Onstott, R. G. (1992). SAR and Scatterometer Signatures of Sea Ice. In: F. D. Carsey (Ed.). *Microwave remote sensing of sea ice, Geophysical monograph 68* (pp. 73-104). Washington DC: American Geophysical Union.

Polder, D. & J. H. Van Santen (1946). The Effective Permeability of Mixtures of Solids, *Physica XII*(5), 257-271.

RADARSAT Data Products Specifications (2000). RSI-GS-026, Revision 3/0, May 8, 2000. RADARSAT International.

Reber, B., C. Mätzler, & E. Scanda (1987). Microwave Signatures of Snow Crusts - Modelling and Measurements. International Journal of Remote Sensing 8(11), pp. 1649-1665.

Sass, B. H. N. W. Nielsen, J. U. Jørgensen, B. Amstrup, M. Kmit & K. S. Mogensen (2002). The Operational DMI-HIRLAM System 2002-Version. *Danish Meteorological Institute Technical Report 02-05*, 58 pp. Copenhagen, Denmark.

Schanda, E. (1987). Microwave modelling of snow and soil. *Journal of Electromagnetic Waves and Applications 1*(1), 1-24.

Serreze, M. C., & R. G. Barry (1988). Synoptic activity in the Arctic Basin, 1979-85. *Journal of Climate 1*, 1276-1295.

Sheperd, N. (1998). Extraction of Beta Nought and Sigma Nought from RADARSAT CDPF Products. ALTRIX Systems Report No. AS97-5001, 8 pp.

Shokr, M. E. (1998). Field Observations and Model Calculations of Dielectric Properties of Arctic Sea Ice in the Microwave C-band. *IEEE transactions on Geoscience and Remote Sensing 36*(2), pp. 463-478.

Srivastava, S. K., B. T. Banik, M. Adamovic and R. Gray (1999). Maintaining Image Quality and Calibration of RADARSAT-1 CDPF Products. *Procedings of the International Geoscience and Remote Sensing Symposium*, pp. 443-445. Hamburg, Germany.

Steffen, K., J. Key, D. J. Cavalieri, J. Comiso, P. Gloersen, K. S. Germain, & I. Rubinstein (1992). The estimation of geophysical parameters using passive microwave algorithms. In: F. D. Carsey (Ed.). *Microwave remote sensing of sea ice, Geophysical monograph 68* (pp. 201-231). Washington DC: American Geophysical Union.

Stiles, W. H. & F. T. Ulaby (1980). The Active and Passive Microwave Response to Snow Parameters 1. Wetness. *Journal of Geophysical Research 85*(C2), 1037-1044.

Stogryn, A. (1986). A study of the Microwave Brightness Temperature of Snow from the Point of View of Strong Fluctuation Theory. *IEEE Transactions on Geoscience and Remote Sensing 24*(2), pp. 220-231.

Svendsen, E., C. Mätzler, & T.C. Grenfell (1987). A model for Retrieving Total Sea Ice Concentration from Spaceborne Dual-Polarized Passive Microwave Instrument Operating Near 90 GHz. *International Journal of Remote Sensing 8*(10), pp. 1479-1487.

Thompson, D. W. J., & J. M. Wallace (1998). The Arctic Oscillation in the wintertime geopotential height and temperature fields. *Geophysical Research Letters 25*(9), 1 297-1 300.

Tjuatja, S. A. K. Fung & J. Bredow (1992). A Scattering Model for Snow-Covered Sea Ice. *IEEE Transactions on Geoscience and Remote Sensing 30*(4), pp. 805-810.

Tucker, W. B., D. K. Perowich, A. J. Gow, W. F. Weeks, & M. R. Drinkwater (1992). Physical properties of sea ice relevant to remote sensing. In: F. D. Carsey (Ed.). *Microwave remote sensing of sea ice, Geophysical monograph 68* (pp. 9-28). Washington DC: American Geophysical Union.

Ulaby, F. T., R. K. Moore & A. K. Fung (1981). *Microwave Remote Sensing, Fundamentals and Radiometry, vol. 1.* Dedham MA: Artech House.

Ulaby, F. T., R. K. Moore & A. K. Fung (1986). *Microwave Remote Sensing, From Theory to Applications, vol. 3.* Dedham MA: Artech House.

Ulander, L. M. H., A. Carlström & J. Askne (1995). Effects of Frost Flowers, Rough Saline Snow and Slush on the ERS-1 SAR Backscatter of Thin Arctic Sea-Ice. *International Journal of Remote Sensing 16*(17), pp. 3287-3305.

Vant, M. R., R. O. Ramseier & V. Makios (1978). The omplex-Dielectric Constant of Sea Ice at Frequencies in the Range 0.1-40GHz. *Journal of Applied Physics 49*(3), pp.1264-1280.

Voss, S. (2002). Synergetische Charakterisierung von Meereis mit SSM/I- und Scatterometerdaten. (Ph.D.-thesis in German), *Berichte aus dem Institut für Umweltphysik, Band 15*, Universität Bremen, Logos Verlag: Berlin.

Wadhams, P. (1981). The Ice Cover in the Greenland and Norwegian Seas. *Reviews of Geophysics and Space Physics 19*(3), pp. 345-393.

Wadhams, P. (1986). The Seasonal Ice Zone. In: N. Untersteiner (Ed.) *The Geophysics of Sea Ice*. (pp. 825-992) NATO ASI series, series B: Physics Vol. 146. New York and London: Plenum Press.

Wiesmann, A. & C. Mätzler (1999). Microwave Emission Model of Layered Snowpacks. Remote Sensing of Environment 70, pp. 307-316.

Winebrenner, D. P., E. D. Nelson, R. Colony & R. D. West (1994). Observations of Melt Onset on Multiyear Arctic Sea Ice Using the ERS 1 Synthetic Aperture Radar. *Journal of Geophysical Research 99*(C11), pp. 22425-22441.

Winebrenner, D. P., J. Bredow, A. K. Fung, M. R. Drinkwater, S. Nghiem, A. J. Gow, D. K. Perowich, T. C. Grenfell, H. C. Han, J. A. Kong, J. K. Lee, S. Mudaliar, R. G. Onstott, L. Tsang, R. D. West (1992). Microwave Sea Ice Signature Modelling. In: F. D. Carsey (Ed.). *Microwave remote sensing of sea ice, Geophysical monograph 68* (pp. 137-175). Washington DC: American Geophysical Union.

DANISH METEOROLOGICAL INSTITUTE

Scientific Reports

Scientific reports from the Danish Meteorological Institute cover a variety of geophysical fields, i.e. meteorology (including climatology), oceanography, subjects on air and sea pollution, geomagnetism, solar-terrestrial physics, and physics of the middle and upper atmosphere.

Reports in the series within the last five years:

No. 99-1
Henrik Feddersen: Project on prediction of climate variations on seasonel to interannual timescales (PROVOST) EU contract ENVA4-CT95-0109: DMI contribution to the final report: Statistical analysis and post-processing of uncoupled PROVOST simulations

No. 99-2
Wilhelm May: A time-slice experiment with the ECHAM4 A-GCM at high resolution: the experimental design and the assessment of climate change as compared to a greenhouse gas experiment with ECHAM4/OPYC at low resolution

No. 99-3
Niels Larsen et al.: European stratospheric monitoring stations in the Artic II: CEC Environment and Climate Programme Contract ENV4-CT95-0136. DMI Contributions to the project

No. 99-4
Alexander Baklanov: Parameterisation of the deposition processes and radioactive decay: a review and some preliminary results with the DERMA model

No. 99-5
Mette Dahl Mortensen: Non-linear high resolution inversion of radio occultation data

No. 99-6
Stig Syndergaard: Retrieval analysis and methodologies in atmospheric limb sounding using the GNSS radio occultation technique

No. 99-7
Jun She, Jacob Woge Nielsen: Operational wave forecasts over the Baltic and North Sea

No. 99-8
Henrik Feddersen: Monthly temperature forecasts for Denmark - statistical or dynamical?

No. 99-9
P. Thejll, K. Lassen: Solar forcing of the Northern hemisphere air temperature: new data

No. 99-10
Torben Stockflet Jørgensen, Aksel Walløe Hansen: Comment on "Variation of cosmic ray flux and global coverage - a missing link in solar-climate relationships" by Henrik Svensmark and Eigil Friis-Christensen

No. 99-11
Mette Dahl Meincke: Inversion methods for atmospheric profiling with GPS occultations

No. 99-12
Hans-Henrik Benzon; Laust Olsen; Per Høeg: Simulations of current density measurements with a Faraday Current Meter and a magnetometer

No. 00-01
Per Høeg; G. Leppelmeier: ACE - Atmosphere Climate Experiment

No. 00-02
Per Høeg: FACE-IT: Field-Aligned Current Experiment in the Ionosphere and Thermosphere

No. 00-03
Allan Gross: Surface ozone and tropospheric chemistry with applications to regional air quality modeling. PhD thesis

No. 00-04
Henrik Vedel: Conversion of WGS84 geometric heights to NWP model HIRLAM geopotential heights

No. 00-05
Jérôme Chenevez: Advection experiments with DMI-Hirlam-Tracer

No. 00-06
Niels Larsen: Polar stratospheric clouds microphysical and optical models

No. 00-07
Alix Rasmussen: "Uncertainty of meteorological parameters from DMI-HIRLAM"

No. 00-08
A.L. Morozova: Solar activity and Earth's weather. Effect of the forced atmospheric transparency changes on the troposphere temperature profile studied with atmospheric models

No. 00-09
Niels Larsen, Bjørn M. Knudsen, Michael Gauss, Giovanni Pitari: Effects from high-speed civil traffic aircraft emissions on polar stratospheric clouds

No. 00-10
Søren Andersen: Evaluation of SSM/I sea ice algorithms for use in the SAF on ocean and sea ice, July 2000

No. 00-11
Claus Petersen, Niels Woetmann Nielsen: Diagnosis of visibility in DMI-HIRLAM

No. 00-12
Erik Buch: A monograph on the physical oceanography of the Greenland waters

No. 00-13
M. Steffensen: Stability indices as indicators of lightning and thunder

No. 00-14
Bjarne Amstrup, Kristian S. Mogensen, Xiang-Yu Huang: Use of GPS observations in an optimum interpolation based data assimilation system

No. 00-15
Mads Hvid Nielsen: Dynamisk beskrivelse og hydrografisk klassifikation af den jyske kyststrøm

No. 00-16
Kristian S. Mogensen, Jess U. Jørgensen, Bjarne Amstrup, Xiaohua Yang and Xiang-Yu Huang: Towards an operational implementation of HIRLAM 3D-VAR at DMI

No. 00-17
Sattler, Kai; Huang, Xiang-Yu: Structure function characteristics for 2 meter temperature and relative humidity in different horizontal resolutions

No. 00-18
Niels Larsen, Ib Steen Mikkelsen, Bjørn M. Knudsen m.fl.: In-situ analysis of aerosols and gases in the polar stratosphere. A contribution to THESEO. Environment and climate research programme. Contract no. ENV4-CT97-0523. Final report

No. 00-19
Amstrup, Bjarne: EUCOS observing system experiments with the DMI HIRLAM optimum interpolation analysis and forecasting system

No. 01-01
V.O. Papitashvili, L.I. Gromova, V.A. Popov and O. Rasmussen: Northern polar cap magnetic activity index PCN: Effective area, universal time, seasonal, and solar cycle variations

No. 01-02
M.E. Gorbunov: Radioholographic methods for processing radio occultation data in multipath regions

No. 01-03
Niels Woetmann Nielsen; Claus Petersen: Calculation of wind gusts in DMI-HIRLAM

No. 01-04
Vladimir Penenko; Alexander Baklanov: Methods of sensitivity theory and inverse modeling for estimation of source parameter and risk/vulnerability areas

No. 01-05
Sergej Zilitinkevich; Alexander Baklanov; Jutta Rost; Ann-Sofi Smedman, Vasiliy Lykosov and Pierluigi Calanca: Diagnostic and prognostic equations for the depth of the stably stratified Ekman boundary layer

No. 01-06
Bjarne Amstrup: Impact of ATOVS AMSU-A radiance data in the DMI-HIRLAM 3D-Var analysis and forecasting system

No. 01-07
Sergej Zilitinkevich; Alexander Baklanov: Calculation of the height of stable boundary layers in operational models

No. 01-08
Vibeke Huess: Sea level variations in the North Sea – from tide gauges, altimetry and modelling

No. 01-09
Alexander Baklanov and Alexander Mahura: Atmospheric transport pathways, vulnerability and possible accidental consequences from nuclear risk sites: methodology for probabilistic atmospheric studies

No. 02-01
Bent Hansen Sass and Claus Petersen: Short range atmospheric forecasts using a nudging procedure to combine analyses of cloud and precipitation with a numerical forecast model

No. 02-02
Erik Buch: Present oceanographic conditions in Greenland waters

No. 02-03
Bjørn M. Knudsen, Signe B. Andersen and Allan Gross: Contribution of the Danish Meteorological Institute to the final report of SAMMOA. CEC contract EVK2-1999-00315: Spring-to.-autumn measurements and modelling of ozone and active species

No. 02-04
Nicolai Kliem: Numerical ocean and sea ice modelling: the area around Cape Farewell (Ph.D. thesis)

No. 02-05
Niels Woetmann Nielsen: The structure and dynamics of the atmospheric boundary layer

No. 02-06
Arne Skov Jensen, Hans-Henrik Benzon and Martin S. Lohmann: A new high resolution method for processing radio occultation data

No. 02-07
Per Høeg and Gottfried Kirchengast: ACE+: Atmosphere and Climate Explorer

No. 02-08
Rashpal Gill: SAR surface cover classification using distribution matching

No. 02-09
Kai Sattler, Jun She, Bent Hansen Sass, Leif Laursen, Lars Landberg, Morten Nielsen og Henning S. Christensen: Enhanced description of the wind climate in Denmark for determination of wind resources: final report for 1363/00-0020: Supported by the Danish Energy Authority

No. 02-10
Michael E. Gorbunov and Kent B. Lauritsen: Canonical transform methods for radio occultation data

No. 02-11
Kent B. Lauritsen and Martin S. Lohmann: Unfolding of radio occultation multipath behavior using phase models

No. 02-12
Rashpal Gill: SAR ice classification using fuzzy screening method

No. 02-13
Kai Sattler: Precipitation hindcasts of historical flood events

No. 02-14
Tina Christensen: Energetic electron precipitation studied by atmospheric x-rays

No. 02-15
Alexander Mahura and Alexander Baklanov: Probablistic analysis of atmospheric transport patterns from nuclear risk sites in Euro-Arctic Region

No. 02-16
A. Baklanov, A. Mahura, J.H. Sørensen, O. Rigina, R. Bergman: Methodology for risk analysis based on atmospheric dispersion modelling from nuclear risk sites

No. 02-17
A. Mahura, A. Baklanov, J.H. Sørensen, F. Parker, F. Novikov K. Brown, K. Compton: Probabilistic analysis of atmospheric transport and deposition patterns from nuclear risk sites in russian far east

No. 03-01
Hans-Henrik Benzon, Alan Steen Nielsen, Laust Olsen: An atmospheric wave optics propagator, theory and applications

No. 03-02
A.S. Jensen, M.S. Lohmann, H.-H. Benzon and A.S. Nielsen: Geometrical optics phase matching of radio occultation signals

No. 03-03
Bjarne Amstrup, Niels Woetmann Nielsen and Bent Hansen Sass: DMI-HIRLAM parallel tests with upstream and centered difference advection of the moisture variables for a summer and winter period in 2002

No. 03-04
Alexander Mahura, Dan Jaffe and Joyce Harris: Identification of sources and long term trends for pollutants in the Arctic using isentropic trajectory analysis

No. 03-05
Jakob Grove-Rasmussen: Atmospheric Water Vapour Detection using Satellite GPS Profiling

No. 03-06
Bjarne Amstrup: Impact of NOAA16 and NOAA17 ATOVS AMSU-A radiance data in the DMI-HIRLAM 3D-VAR analysis and forecasting system - January and February 2003

No. 03-07
Kai Sattler and Henrik Feddersen: An European Flood Forecasting System EFFS. Treatment of uncertainties in the prediction of heavy rainfall using different ensemble approaches with DMI-HIRLAM

No. 03-08
Peter Thejll and Torben Schmith: Limitations on regression analysis due to serially correlated residuals: Application to climate reconstruction from proxies

No. 03-09
Peter Stauning, Hermann Lühr, Pascale Ultré-Guérard, John LaBrecque, Michael Purucker, Fritz Primdahl, John L. Jørgensen, Freddy Christiansen, Per Høeg, Kent B. Lauritsen: OIST-4 Proceedings. 4'th Oersted International Science Team Conference. Copenhagen 23-27 September 2002

No. 03-10
Niels Woetmann Nielsen: A note on the sea surface momentum roughness length.

No. 03-11
Niels Woetmann Nielsen: Quasigeostrophic interpretation of extratropical cyclogenesis